Latest Developments in 3D-Printed Engineered Cementitious Composites: Technologies, Prospects, and Challenges

ceramics

MDPI

Review

Latest Developments in 3D-Printed Engineered Cementitious Composites: Technologies, Prospects, and Challenges

Jean-Marc Tulliani

Department of Applied Science and Technology, INSTM R.U. Lince Laboratory, Politecnico di Torino, Corso Duca degli Abruzzi, 24, 10129 Torino, Italy; jeanmarc.tulliani@polito.it

Abstract

Engineered cementitious composites (ECCs) are fiber-reinforced materials with enhanced tensile strength, ultra-high ductility, crack resistance, and long-term durability. This review aims to explore the latest developments when combining ECC and 3D printing in depth. It will analyze the main technologies used, the specific properties of the materials employed, the results achieved so far, and the challenges still to be addressed for the wider deployment of these innovative solutions. The goal is to provide a comprehensive and up-to-date overview, highlighting the potential of this technology.

Keywords: engineered cementitious composites; ECC; 3D printing; 3D-printable strain-hardening cementitious composites; 3D-SHCCs; mechanical properties

Academic Editor: Malika Saadaoui

Received: 27 September 2025
Revised: 6 November 2025
Accepted: 17 November 2025
Published: 23 November 2025

Citation: Tulliani, J.-M. Latest Developments in 3D-Printed Engineered Cementitious Composites: Technologies, Prospects, and Challenges. *Ceramics* **2025**, *8*, 141. https://doi.org/10.3390/ceramics8040141

1. Introduction

Concrete is by far the most used construction material on Earth, and it is characterized by a high compressive strength as well as a low tensile strength (corresponding to about 10–12% of the compressive strength) [1]. Thus, fibers have been added to concrete mixes for more than 60 years to increase the fracture toughness of hardened materials. In this case, the resistance against cracking is improved by controlling crack opening and propagation [2,3]. When opening cracks are bridged by fibers, then debonding, fiber fracture, and fiber pull-out may happen between fibers and the matrix at rupture, leading to pseudo post-cracking ductility on stress–strain curves and decreasing brittleness. The tensile strength of composite materials can also be increased due to the presence of fiber reinforcement. Engineered cementitious composites (ECCs) or Strain-Hardening Cementitious Composites (SHCCs) [4] or bendable concretes are fiber-reinforced high-performance materials designed by Prof. Victor Li and co-workers [5] at the University of Michigan in the 1990s. These materials have ultra-high tensile ductility and crack widths limited to less than 100 μm, combined with an ultimate tensile strain capacity of more than 3%, while keeping a fiber volume fraction below 2% [6], as shown in Figure 1. These features are obtained by the addition of high-strength fibers into the cementitious matrix, which dissipate the fracture energy, distribute and limit crack apertures when the material is under stress, and prevent sudden brittle failure under tensile loads [7]. The mechanical concept behind SHCCs/ECCs is the following: when the first initial microcrack appears, the fibers supply the tensile force. Then, when the fibers bridge the crack, the force equilibrium of the damaged element is restored. If the applied force rises again, a new crack will appear at a different place, and the same mechanism repeats. This process happens repeatedly, until the tensile force within the concrete specimen surpasses the fiber bridging capacity of the formed cracks. At that point, the crack will be localized, leading to material failure. This mechanism can

be activated if two micro-mechanical conditions are fulfilled: the matrix cracking strength is lower than the maximum fiber bridging capacity of the already formed cracks, and the fiber can bridge the matrix crack [8]. When the fiber/matrix interface is too weak, the fibers are simply pulled out, while when the interface is too strong, the fibers break. In these cases, the complementary energy will not be enough to create a steady-state crack, and the composite will rather display a strain softening behavior. On the contrary, for strain-hardening behavior, it is of paramount importance that the fiber has just enough freedom to deform. Then, only in this condition, complementary energy is needed to reach a steady-state crack propagation and the corelated strain-hardening behavior [8].

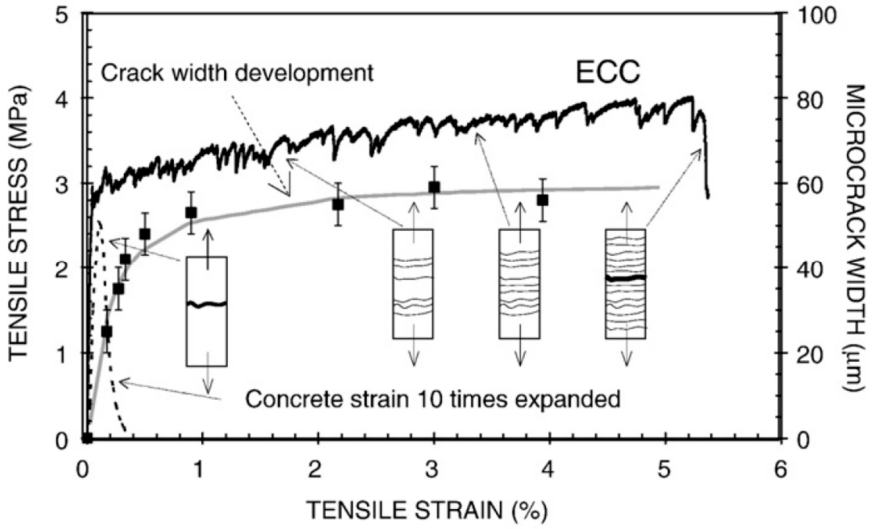

Figure 1. Tensile stress–strain curve of an ECC compared to a traditional concrete. In ECC, when the first microcrack appears, fibers supply the tensile force and bridge it. When further increasing the applied force, a new crack will appear at a different place, and the same mechanism repeats. This process goes on until the tensile force within the concrete specimen is higher than the fiber bridging capacity of the formed cracks. Then, the crack will be localized, leading to material failure. Thus, the strain value is 300–500 times higher than that of concrete. Reprinted from ref. [9] with permission from Elsevier.

ECC is in fact a family of materials that display different tensile strengths and ductility values adapted for a particular structure due to a design based on micromechanical theory (Table 1).

Table 1. Main properties of ECC [6].

Compressive Strength (MPa)	First Crack Strength (MPa)	Ultimate Tensile Strength (MPa)	Ultimate Tensile Strain (%)	Young's Modulus (GPa)	Flexural Strength (MPa)	Density (g/cm^3)
20–150	3–10	4–20	3–12	18–40	10–50	0.95–2.3

ECC can be used in new constructions and structures in place of conventional concrete for structural elements such as beams, walls, and columns. The high ductility of ECC notably increases the element's capacity to absorb impact energy, limiting structural damage. Thus, ECC coupling beams have been proposed in place of reinforced-concrete coupling beams for tall building designs in Europe, Japan, and the United States (like the Glorio-Tower, a 27-story structure located in central Tokyo, the Nabule Yokohama Tower, a 41-story skyscraper situated in Yokohama, and the Kitahama Tower, a 60-story tower located in Osaka) [10]. In addition, infrastructural elements, such as water irrigation channels, dams,

and road pavements, also use ECC to increase their operational efficiency and increase their lifespan [7]. The water permeability of ECC can be effectively controlled during the strain-hardening phase thanks to its limited crack width [11].

ECC's composition can be adapted to many structural requirements: blast resistance ability is guaranteed by high-tensile-strength ECC, while building damper properties are reached by high-compressive-strength ECC, and structural durability is ensured by tight-crack ECC [12]. Thus, using ECC guarantees increased service life, improved functionalities such as leak-proofing and energy absorption, and limiting installed costs [13]. In the case of earthquakes or to decrease the brittleness of building materials, ECC can be useful for several structural applications too. ECCs present high ductility and toughness, which make them ideal candidates for scenarios where elevated deformations and cracking resistance are requested. The use of ECC within the plastic connection zone in place of concrete and as a partial replacement for transverse reinforcement can significantly increase energy absorption capacity, joint shear resistance, and cracking response. Moreover, joint seismic resistance will be increased while simultaneously reducing reinforcement congestion, simplifying the construction [14]. Experimental results demonstrated that polypropylene fiber-reinforced ECC was able to replace transverse reinforcements in the beam–column links of railway rigid-framed bridges [15].

Several review papers on ECCs are available in the literature and deal with material properties and applications [11,16,17], durability in various environments [18], structural design and performance [19], and self-healing properties [20].

The strain-hardening ability of ECCs makes them appeal also for 3D concrete printing techniques. While conventional printable mortars show brittle failure when submitted to tensile loads, ECCs can withstand them, making them much safer for structural applications [21]. Pioneering works on 3D-printed ECCs showed promising results. Actually, printed concrete structures often need post-tensioning systems for reinforcement [22,23]. While these systems introduce positive compressive stresses in the printed materials, they also generate tensile stresses perpendicular to the direction of reinforcement [24].

Thus, this review aims to explore the latest developments when combining ECCs and 3D printing in depth. It will analyze the main technologies used, the specific properties of the materials employed, the results achieved so far, and the challenges still to be addressed for the wider deployment of these innovative solutions. The goal is to provide a comprehensive and up-to-date overview, highlighting the potential of this technology able to revolutionize how we design and build our environment.

2. Composition of ECC

The composition of ECC includes fibers, fine aggregates, cement, water, supplementary cementitious materials (SCMs), and admixtures [7]. The first ECC materials relied on high-modulus polyethylene (PE) fibers and reached a compressive strength of 65.6 MPa, with a tensile strain capacity of 5.6% [25]. Then, in the early 2000s, Li et al. [26] replaced PE fibers with polyvinyl alcohol (PVA) ones for manufacturing ECCs for structural applications. These new materials showed a tensile strength and strain capacity of up to 5.0 MPa and 4.6%, respectively. To prevent PVA fiber breakage in the cementitious matrix as a result of strong chemical bonding, their surface was coated with oil [27].

Fibers can have different features, shapes, and sizes. However, their selection should be carried out with attention, as glass, basalt, and recycled polyethylene terephthalate fibers can be degraded over time due to the high pH value of cementitious materials [28–30]. Fibers can lower the total cost of the construction of concrete structures, as they can replace traditional rebars [29,31]. In addition, the labor and maintenance costs will be reduced, as well as time during the phase of the structure's construction and the final building. The

embodied energy of the structure (the energy needed to produce a material or a building, from the quarrying and processing of natural resources to production, transport, and product delivery) will be lowered too, as the amount of added fibers is much lower than the volume of steel used for traditional rebars. Incorporating recycled fibers from waste materials is also a possible option [32].

Different kinds of fibers such as PVA, PE, and steel (SF) fibers have been proposed alone or to be used in combination for manufacturing ECCs [6]. Recently, polyvinyl-pyrrolidone-modified [33] or ethylene–vinyl acetate modified [34] polyethylene fibers and aramid nanofibers derived from recycled aramid fibers [35] were also proposed. However, the cost and availability of aramid fibers should be assessed for real constructions and not only for laboratory testing. Hybrid fibers with high- and low-modulus fibers can also be employed to reach an optimal balance between ultimate strength, crack width, and strain capacity [6,26,36–40]. Carbon fibers induce a low tensile ductility in cementitious materials, as the strain capacity is below 1%. However, they can be used to develop multifunctional cementitious materials because they are electrically conducting [41].

Recycled polyethylene terephthalate (PET) fibers were also investigated; however, chemical degradation concerns in alkaline environments remain even if physical and mechanical properties of fibers can be improved [42]. Natural fibers, like banana stem, coconut, Curauá, sisal, and bagasse fibers, were also studied in cementitious materials, though their durability is expected to be weak [42–44].

In composite materials, interfaces are of paramount importance during stress transfer between the fibers and the matrix. Thus, fibers for the production of ECCs must fulfill these requirements [41]:

- Amount $\leq$ 2 vol%;
- Diameter from 20 to 50 μm;
- Length from 6 to 12 mm; increasing fiber length leads to poorer printability;
- Tensile strength $\geq$ 800 MPa;
- Elastic tensile modulus $\geq$ 10 GPa;
- Tensile strain capacity $\geq$ 3%;
- Limited or no interfacial chemical bond;
- Interfacial frictional bond from 1 to 6 MPa, depending on fiber strength;
- Enough corrosion resistance and chemical stability in cementitious systems;
- Stability of properties over time.

The recommended fiber diameter values lead to high aspect ratios, which favor polymeric fibers because of their production techniques. Lower diameter values limit too large aspect ratios (~300) that would reduce workability and hamper fiber dispersion. The fiber tensile strength governs fiber rupture and the maximum bridging stress σ_0 (initial crack sizes must be smaller than the fiber bridging capacity, σ_0) [45,46], while the fiber tensile modulus is less important in the ECC's mechanical properties before cracking. However, this modulus is important to limit the crack aperture in damaged materials [45,46]. Another critical feature is the fiber tensile strain capacity to prevent failure when mixing [47]. Fiber rupture during the mixing step reduces the fiber length and aspect ratio and limits the ECC's reinforcing performance. Moreover, fiber breakage in hardened composites is challenging for randomly oriented low-shear-strain fibers when they need to bend during microcrack bridging. For example, when forming a certain angle, most carbon fibers with a low shear strain capacity can break. Therefore, metallic and polymeric fibers perform better in this particular condition [48–50].

Fiber/matrix interfacial bonding is a key point to ensure the mechanical performance of ECCs. With a limited interfacial bond, the crack bridging ability is reduced, allowing fibers to slip out, conferring to the composite low tensile ductility and large crack widths.

On the contrary, if the bond is too strong, fibers have a tendency to break instead of sliding out, decreasing the energy absorption and strain capacity of the composite [51]. Polymeric fibers usually have low bond strengths (below 1 MPa), with the exception of PVA fibers that present a frictional bond ranging from 2 to 5 MPa. This high interfacial bond can be reduced by coating them with oil.

PVA fibers can be used to limit an excessive fiber breakage and loss of tensile ductility [27]. The targeted range of the interfacial bond is also a function of the fiber length, diameter and strength [47].

Fibers also contribute to increasing the surface area to be wet, thereby decreasing the availability of free water to lubricate cement grains, specifically for PVA fibers that are hydrophilic and have low density. On the contrary, PE fibers are usually hydrophobic and do not reduce the amount of free water in the mix, displaying a different behavior [52].

In general, lower fiber volume fractions, shorter fibers, lower w/b ratios, or nanoclay addition improve the printability of ECCs [53].

Finally, the chemical stability of fibers is of paramount importance to maintain the composites' performance over time. It is obvious that carbon and polymeric fibers are much more corrosion-resistant than steel fibers, especially if stainless or galvanized steel fibers are not used [54]. Concerning chemical stability, carbon fibers are usually inert, while some polymeric and glass fibers can degrade or undergo aging phenomena due to the high basicity of the cement paste [54]. Fibers density is not crucial due to the rather low fiber volume fraction in ECC [47]. However, since the cost of fibers is based on a unit mass, while their reinforcing effectiveness is estimated in volume [10], considering the same fiber volume fraction, high-density fibers tend to weigh and cost more than a corresponding low-density fibers.

To sum up, the key points related to fiber properties and contents for ECC production are as follows:

- PE and PVA fibers that are 20–50 μm in Ø are commonly used for ECC manufacturing;
- Recycled aramid nanofibers seem promising as well;
- High aspect ratios are needed;
- A high tensile strength and a rather low bond strength with the cementitious matrix are desirable;
- Common dosages are 1–2 vol%;
- Chemical stability in high-pH environments is mandatory.

3. Printing Processes with Concrete

Nowadays, the use of 3D-printed concrete technology is mostly restricted to formwork printing (i.e., contouring process [55]) because of concrete's low tensile strength, poor ductility, and brittleness [56]. Thus, reinforcing techniques, such as prestressing, wire mesh, and simultaneous printing of steel bars, have been investigated [57–59]. However, all these techniques require additional labor and energy input, which is inefficient and incoherent with the 3D printing process of concrete (3DPC). Therefore, fiber addition before printing allows for self-reinforcement of the composite and makes ECCs highly compatible with 3DPC [52].

Common concrete printing methods include extrusion- and powder-based methods. In the extrusion-based technique, the raw materials are pre-mixed and extruded layer-by-layer. A high viscosity is required to confer low slump and self-support abilities, which makes this process close to extrusion. The mix must be extrudable and robust enough to maintain its shape during printing. In the powder-based technique, the raw materials are divided into two parts: on one side are the liquids, and on the other side are the powders. The liquids are dripped to the desired position by the printer layer-by-layer on the powder

bed made of cement, fly ash, sand, etc. Thus, the liquid and powder parts are printed alternatively, which is another difference between the two techniques [60–64]. Optimal contact between the liquid and the powder parts is crucial for the quality of the printed parts. In the case of 3D-printed ECCs, only the extrusion-based method is used due to the presence of fibers.

The 3DPC process is shown in Figure 2.

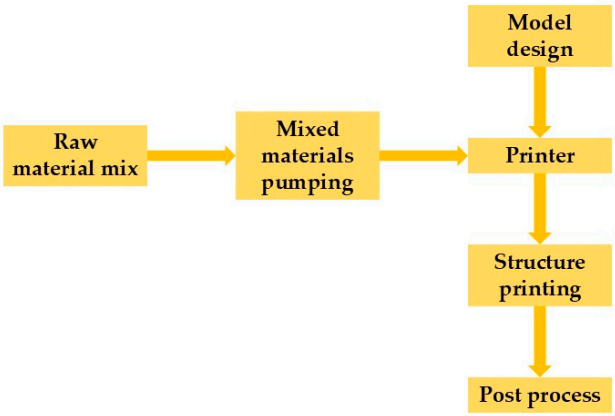

Figure 2. Flow chart of 3DPC. Figure adapted from ref. [60]. Licensed under CC BY 4.0.

In addition to the features of the printed mix, the ability of the printers and printing parameters are also important. For example, the extrusion speed should match the printing speed to control the shape and quality of printed filaments [65]. A reduced extrusion rate can produce thin layers, or even worse, discontinuous layers, while a very high speed can lead to hose blockage. In addition, waiting for a long time between printed layers allows the layer below to become too stiff to support the layers printed above, but this also decreases the bond strength between the layers [66]. Generally, printing directions show limited influence, but the distance between the nozzle and printed filaments is important [67]. A shorter distance decreases the time and space for gravity to deform filaments before encountering the bed. The accumulative deformation of each layer reduces the total height and also increases the distance between the nozzle and the last printed filament (standoff distance). Thus, the printing toolpath must be modified periodically to compensate for dynamic errors and maintain this distance. Many printing parameters of extrusion-based printing are reported in [60]. Printed filaments can have a height of 5–25 mm and a width of 30–65 mm. Meanwhile, the printing speed is different in the horizontal (H) and vertical (V) directions. These rates can vary from 20 to 157 mm/s (H) and from 1 to 13 mm/s (V). Finally, the volume of extruded material is in the range from 1 to 29 L/min, or if expressed in mass, it can reach up to 850 kg/h [60].

Several papers have studied the 3D printing process of ECCs [68–71], evidencing the strong potential of these composites as self-reinforcing printable materials [13]. However, some technical problems have still to be solved, as detailed below [21].

The key points when dealing with concrete 3D printing are as follows:

- The extrusion speed should match the printing speed to control the shape and quality of printed filaments;
- Long delays between printing one filament above an existing are not advisable;
- The standoff distance should be kept constant throughout the process.

4. Extrusion Process and Fresh State Properties

4.1. Mixing Procedure

Figure 3 shows the mix preparation procedure of a 3D-printed ECC (3DP-ECC) [72]. All the solids (binder, sand, fly ash (FA), silica fume (SF), and superplasticizer (SP)) were first premixed for 1 min. Then, 90% of the mixing water was added, and the mix was stirred for 2 min. The PE fibers were divided into three equal amounts, each one added after a 3 min mixing time step. The remaining part of the water was finally added to the mix once a uniform fiber dispersion was reached. The mixing speed was maintained constant at 48 rpm during the whole process. The fresh mixture of PE-ECC was transferred directly from the mixer to the material hopper of the 3D printer at a time of 20 min after the addition of the first batch of water.

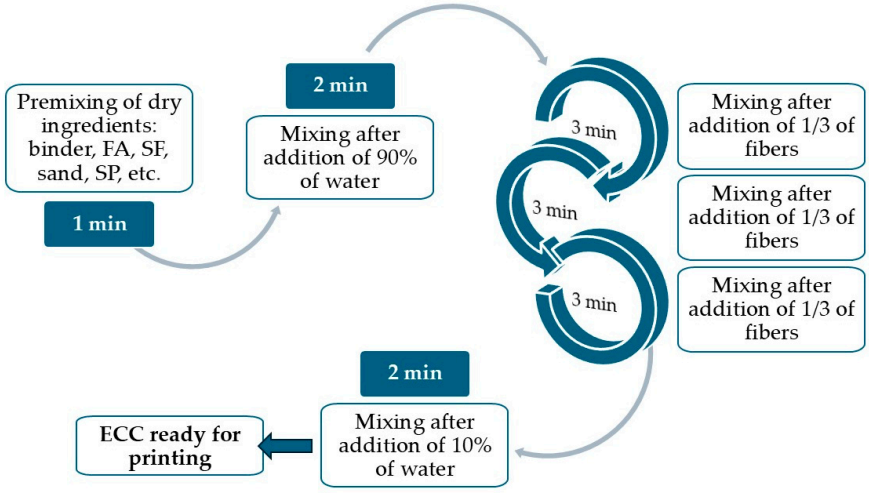

Figure 3. Mix preparation procedure of 3DP-ECC. Figure adapted from ref. [72].

In ref. [73], all the solids (binders + sand) are mixed at 140 rpm for 120 s, then water and SP are added, and the wet mix is stirred at 140 rpm for 180 s. At this point, the HPMC powder is poured and mixed for 60 s. PE fibers are added gradually while the stirring speed is raised to 420 rpm. A similar procedure was also used in ref. [69] with PVA fibers.

A slightly different mixing sequence is shown in [74], where presoaked pumice lightweight aggregates are proposed as internal curing agents. Mixing was performed in four steps (Figure 4). First, the solids (binders (cement + GGBFS) and fine aggregates) were mixed for 5 min at a low speed (140 ± 5) rpm. Then, a solution of water and SP (high-range water-reducing agent, HRWRA) was poured into the dry mix and mixed for 3 more min. At this point, presoaked pumice aggregates were added into the wet mix. Finally, PE fibers were supplemented, and mixing went on for 5 min at a low speed, (140 ± 5) rpm, before switching to a high speed, (285 ± 10) rpm, for 5 min.

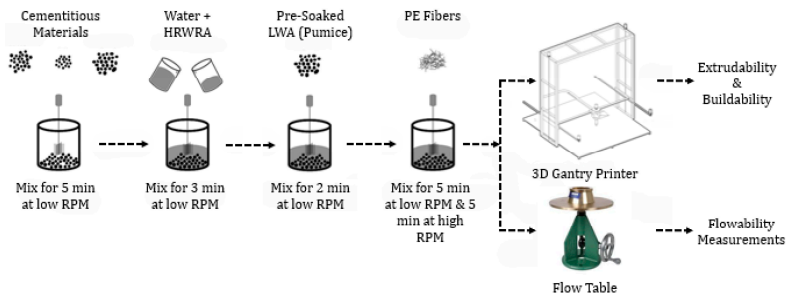

Figure 4. Mix preparation procedure of 3DP-ECCs with presoaked pumice aggregates. Reproduced from Zafar et al., 2025, licensed under CC BY 4.0 [74].

In any case, a common denominator can be found throughout the different mixing procedures: solids are first dry-mixed for 1–2 min, then water and SP are added (totally or only 90% of liquids) and mixed for 2–3 min, while fibers are progressively supplemented and mixed for several minutes at the end of the process. Finally, if remaining liquids are available, they are introduced into the mix.

4.2. Material Features

As for normal concrete, the printing process requires specific features of the material, specifically, the pumpability, extrudability, buildability, and open time (Figure 5). When printing, the material's properties evolve due to hydration reactions; thus, the strength and stiffness of the material continuously increase over time, decreasing its fluidity and increasing its bearing capacity. First, the mix should have a low initial stiffness to be pumped through the printing system and extruded, while the buildability requirement needs a material that is strong enough to bear its own weight, as well as the weight of all the successive layers on top. These two requirements are clearly in conflict from the point of view of the fresh material's properties [21].

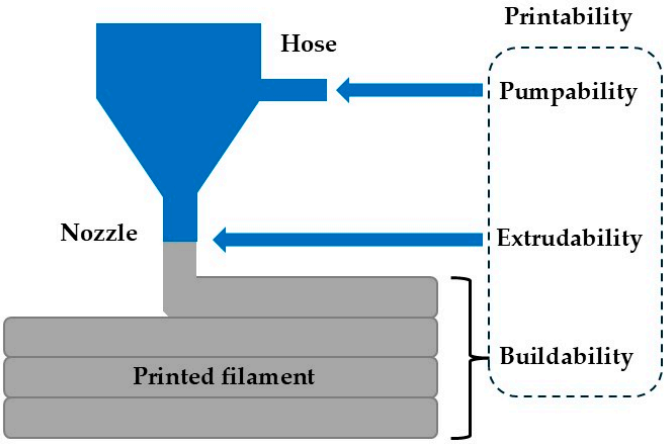

Figure 5. Workability requirements with 3D-printed concrete. Figure adapted from ref. [75]. Licensed under CC BY 4.0.

The open time should be at least 30 min, but several papers have evidenced successful printability for more than 60 min, keeping in mind that 3D printing is a time-sensitive process. The optimal open time is a balance between keeping sufficient flowability for extrusion and satisfying stiffness for buildability and shape retention of each deposited filament [76].

The open time is sometimes defined in two ways:

- Dynamic open time: The material is in the mixer at 140 rpm, simulating its movement in the hopper during the printing process.
- Dynamic–static open time: The material is kept without agitation in the mixer, and agitation is applied at 140 rpm for 30 s before measuring the consistency.

The rheological behavior of the mix is important, as well as its thixotropic character, to better understand what happens during its stay in the hopper [77]. Thixotropic materials present a reduced viscosity under shear stress (during pumping) to guarantee flowability, which suddenly increases when the stress stops (rebuilding process). The thixotropy of the mix is intimately related to its buildability [78]. The complexity of fulfilling all the requirements is well illustrated in the study by Figueiredo et al. [69,79]. The authors first adjusted the fresh material properties by means of admixtures and by varying the water-to-cement (w/c) ratio to meet the requirements of pumpability, extrudability, and open

time. However, this was not sufficient regarding the buildability. Moreover, because of the adaptation of the mechanical properties in the fresh state, the strain-hardening capacity of the ECC was compromised. This was also highlighted by van Overmeir et al. [71], who pointed out the difficulty in satisfying all the requested mechanical properties. In their research, these authors designed ECC mixes with an optimized particle size distribution to guarantee a good packing of particles and sufficient buildability and used a gantry system printing facility with a nozzle with a rectangular cross-section of 40 × 14 mm^2. However, even if some samples possessed a strain-hardening capacity, mechanical tests evidenced that the composites' matrix was too strong to guarantee enough strain-hardening capacity. In general, PVA-reinforced ECCs have a compressive strength of about 40 MPa after 28 days of curing [13,68,80–82]. However, the two studied mix designs showed an average compressive strength of 51 and 56 MPa. Additionally, better buildability led to a reduction in pumpability and print quality, probably due to the arching phenomenon [83,84] in the hopper of the pump. In fact, an arch-like supported mass of bulk material formed in the reservoir pump during gravitational flow, probably due to a high initial yield stress or high thixotropic behavior of the mix. These features did not let the material flow down in the reservoir when the mix underneath was transported by the transport screw. On the contrary, the bulk material formed a self-supported arch, and no material was transferred towards the rotor–stator, producing large air voids [21].

A lack of buildability can reduce the stability and reliability of printed elements: an insufficient buildability can lead to the local failure of the material and overall collapse of the structure [85]. At the material scale, the printed filaments must withstand their own weight and the increasing weight of the successive layers placed on them. Therefore, fast development of the strength and stiffness capacity is needed after filaments are placed [85–88]. Limited and controllable deformation under load facilitates the freshly printed filament to stick to the previous layer and to have sufficient adhesion with it [89]. However, excessive deformation undermines the stability of the structure and results in overall failure. Once the vertical stress in the filament exceeds its capacity, the filament will yield or deform significantly, producing a change in its cross-sectional shape and instability of the structure. At the structural scale, even if the stress in a filament is maintained below the stress threshold, without causing any rupture, the cumulative strain and stress due to all the layers may weaken the shape control and structural stability of the printed part, leading to the collapse of the element, especially in slender structures sensitive to self-buckling [85,89–92]. To estimate the structural failure, Suiker [93] proposed mechanical models that take into consideration elastic buckling failure of printed structures. Roussel [85] calculated the critical height, H_c, at which self-buckling can occur in a slender structure by means of Equation (1):

$$H_c \approx \left(\frac{8EI}{\rho g A}\right)^{\frac{1}{3}} \quad (1)$$

where E is the elastic modulus of the fresh material, I is the moment of inertia, ρ is the density of the fresh material, g is the acceleration of gravity, and A is the horizontal cross-sectional area. The estimated height value can be used to set the nozzle standoff distance when printing and avoid structural instability problems [64].

The simplest method to assess buildability consists of comparing the maximum height or number of filaments that can be piled up under the same printing job settings [94–99]. Nevertheless, printing is needed to assess the buildability of the mix, which consumes time and material. At the same time, vertical strain or deformation of printed filaments also serves as an indirect evaluation index [100–102]. Another strategy is to indirectly estimate the buildability of materials by measuring some of their properties, like green

strength [90,103–108], yield stress [109–112], penetration resistance [111,113] of wet material, etc. The cylinder stability test, where a concrete cylinder is deformed after dynamic tamping or under static loading, has also been proposed to assess shape stability [96]. In ref. [114], the slump value determined according to the ASTM standard C1437−15 (Standard Test Method for Flow of Hydraulic Cement Mortar) was used to assess the buildability of LC3-ECC mixes and was related to the shape retention capacity of a large structure without collapsing during the 3DP process. However, these indicators can only give information at certain time frames, independently from printing parameters [76]. Thus, a quantitative evaluation approach for buildability of 3DP-ECC, considering both the material and the structural scale, is described in [76]. At the material scale, a constant-shear-rate test, incremental loading test, and green strength test were used and showed that the risk of material failure was low, at least for the investigated material compositions [76]. These authors used the following printing parameters: when the structure buildup speed was 3 layers/min over a 0.5 m straight line printed with a nozzle travelling speed of 1.5 m/min, the corresponding uniaxial loading rate was 1.5 N/min. At the same time, for a 10 layers/min buildup rate, the loading speed was around 5 N/min. The mix design was based on 605 kg/m^3 of ordinary Portland cement (OPC), 678 kg/m^3 of FA, 372 kg/m^3 of sand, 1.8 kg/m^3 of SP, a water-to-binder (w/b) ratio of 0.24, and 1.5 vol% of PVA fibers.

At the structural scale, the critical height for self-buckling can be estimated based on the evolution of stiffness over time. Premature self-buckling can be limited by proper design and printing parameters for a given material behavior evolution. The critical height of a printed structure at self-buckling is a function of time (Equation (1)), considering that the elastic modulus of the material can be estimated according to Equation (2):

$$E(t) \approx 2.65 \cdot t + 43 \quad (2)$$

where $E(t)$ is the elastic modulus of the material as a function of time in kPa, and t is the time in min.

According to Kruger et al. [115], printed cementitious materials should have an initial strength in the range from 1 to 10 kPa and a stress development ranging from 0.05 to 0.5 kPa/min during the first 60 min.

A change in printing parameters leads to variation in the microstructure of 3DP-ECC, which, in turn, influences the material's properties (Figure 6).

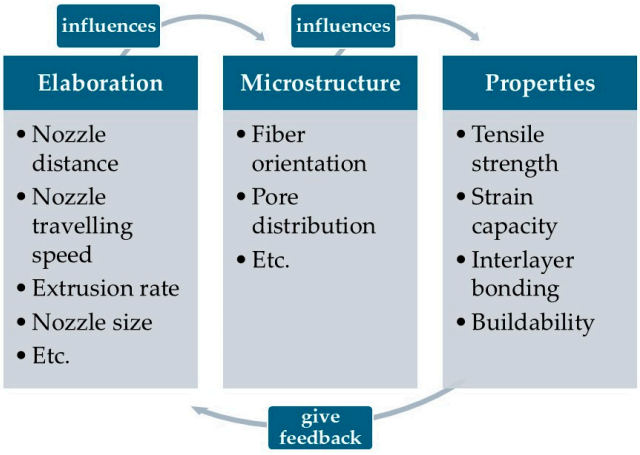

Figure 6. Influence of printing parameters on ECC's microstructure and properties. Figure adapted from ref. [72].

In [77], apart from extrudability and buildability, the workability, another crucial parameter in 3D printing, was evaluated by means of the consistency table according to the

EN 1015–3 standard [10] at 0, 10, 20, 35, 45, and 60 min. A shape retention test was carried out as follows: the freshly extruded mixture was introduced into a mini-slump cone, which was lifted after 1 min. Then, a weight of 465 g was placed on top, and the material was allowed to deform under the load for 45 s. Then, another weight was added to the previous one to reach a final mass of 700 g, and the material was allowed to deform for another 45 s. After each rest time of the mix, the expansion of the material was measured in two directions at 90°. The smaller the diameters, the higher the shape holding capacity of the material [77].

The layer-by-layer printing process produces weak interfaces, which result in a pronounced anisotropy of the structures [5]. Nonetheless, the fibers in 3DP-ECC materials tend to be aligned according to the printing direction, leading to the absence of fiber penetration between layers [6,7]. This anisotropy is higher than in 3DPC. The influence of mix compositions on the fresh properties and anisotropy of 3DP-ECCs, the shape retention ability, and the anisotropy of the compressive strength of 3DP-ECCs with different amounts of fly ash (FA) and hydroxypropyl methyl cellulose (HPMC) were investigated in [116]. HPMC allowed the shape of the printed filaments to be maintained: an addition of 0.35% resulted in a total deformation of 2.67%. HPMC also increased the viscosity and the thixotropy and prevented segregation when pumping [68]. In addition, it acted as a water reservoir when the mix was still fresh and also contributed to the internal curing effect of cementitious composites [79]. Contrarily, when the content of FA increased, the shape retention decreased from 5.3 to 45%. 3DP-ECC materials presented significant anisotropy in terms of compressive strength in different directions according to the following order: z > y > x, with the z direction showing the highest compressive strength, while the x direction had the lowest one [116].

Microsilica, ground silica flour, and attapulgite nanoclay can also be added to improve early strength and thixotropy and enhance cohesion [68]. The silica fume content and the water-to-solid ratio are also important parameters to optimize fresh properties and strain-hardening behavior [117]. Calcium aluminate and sulphoaluminate (CSA) cements can increase the early flowability and the early strength [68]. Sodium silicate can also be used in place of CSA cement, even if its cost is higher, but the effect is strong, and a reduced amount is required to make OPC rapidly set after deposition.

4.3. Influence of Nozzle Size

In [53], three rectangular nozzles with the same cross-sectional area of 150 mm^2 were tested to investigate the effect of the extrusion nozzle size on the 3D printability of a mix made with 0.6 OPC, 0.3 FA, 0.1 microsilica, 0.2 sand, 0–0.5% nanoclay, a 0.325–0.375 w/b and 1–2 vol% PE fibers that were 24 µm in diameter and 9, 12, and 18 mm in length. The nozzle with a smaller width-to-height ratio (5 × 30 mm^2) showed a higher probability of smooth printing with a continuous and non-cracked layer. However, the nozzle size had less influence on fiber agglomeration and clogging in the pump screw.

4.4. Rheological Properties

ECC pastes behave as non-Newtonian fluids. Usually, the Bingham model finds agreement for describing the non-Newtonian fluid rheology of cement pastes (Equation (3)) [117–119]:

$$\tau = \tau_0 + \eta\dot{\gamma} \quad (3)$$

where τ_0 and τ are the yield stress and shear stress, respectively, in Pa; η is the plastic viscosity, in Pa.s; and $\dot{\gamma}$ is the shear rate, in s^{-1}.

Rheological properties can be determined by means of a rheometer. However, the fiber dispersion of ECC significantly impacts its rheological properties. Fibers also increase

the yield stress at rest times, as well as the plastic viscosity and the dynamic yield stress of cementitious composites [52]. Therefore, the printability and fiber dispersion of 3DP-ECC need to be evaluated in a different way.

The yield stress should be lower than the maximum shear force exerted by the extrusion system to guarantee a smooth extrusion process of the mix during printing. At the same time, it should be higher than the weight of the upper extruded filament to maintain its shape. Thus, these two requirements must be fulfilled by the yield stress (Equation (4)) [118]:

$$\rho g h(t) \leq \tau_0 \leq P_{extrusion} \quad (4)$$

where ρ is the density of the mix, in g/cm^3, g is the gravity constant, equal to 9.8 N/kg, $h(t)$ is the height of printed layers, in mm, and $P_{extrusion}$ is the maximum shear force of the printer extrusion system, in Pa. It is also worth mentioning that printed materials commonly contain accelerating agents like sulphate aluminum cement to rapidly confer the extruded filaments enough strength and stiffness. The self-weight pressure of two printed layers can be set as the lower boundary (Equation (5)):

$$\rho g h(2) \leq \tau_0 \leq P_{extrusion} \quad (5)$$

where $h(2)$ is the height of two printed layers, in mm. The theoretical relationship between slump and yield stress was proposed by Hu et al. [120] and is described by Equation (6):

$$\tau_0 = \frac{\rho(H-s)}{0.27} = 3.7 \cdot \rho(H-s) \quad (6)$$

In this way, the yield stress can be related to the slump (Equation (7)):

$$s_1 \leq s \leq s_2 \quad (7)$$

where H is the slump cone's height, in mm; s is the slump, in mm; s_1 represents the lower boundary of the slump, in mm; and s_2 represents the upper boundary of the slump, in mm [121].

In [122], the highest flowability in ECC is achieved with a sand-to-binder (s/b) ratio of 0.35 and a superplasticizer-to-binder (SP/b) ratio of 0.30. The ECC mix with PVA fibers reached a compressive strength of 41.71 MPa after 28 days. This result was due to the good dispersion of fibers within the cementitious matrix during the mixing step thanks to the use of a superplasticizer [122].

To adapt the workability and homogeneity of the fresh mix, two admixtures, i.e., superplasticizer and thickener (or viscosity modifier), must be used [68,123,124]. The thickener changes the rheology of the material and contributes to dispersing the fibers. Then, its influence on tensile properties is high. A high thixotropy is helpful to guarantee that the extruded layers firmly stack up [13]. Therefore, thixotropic additives, like HPMC, can influence printability [73]. The thickener retains water and reduces capillary water absorption [125]. However, its use causes an increase in the void content of about 20 vol% in mortars, which obviously decreases the mechanical properties [126,127]. For example, in [128], the tensile strength and the tensile strain capacity first increased and then decreased with the addition of HPMC, and the optimum value was 0.05%. However, HPMC addition had negative effects on the initial cracking strength and the elastic modulus. When the HPMC content reached 0.05%, the ECC samples showed the ability to saturate multiple cracking, and the crack number, the average crack size, and the average crack spacing almost reached the optimal level. Nevertheless, due to the entrapped air effect of HPMC, the matrix compactness was altered, and the density gradually decreased when increasing

the HPMC content. The matrix fracture toughness was in line with the variations in the initial cracking strength and the compressive strength. The addition of HPMC weakened the frictional bond strength as well as the slip-hardening coefficient during the slippage of fibers from matrix. The effective fiber-bridging effect was the reason for the observed improved tensile properties [128].

Pretreated incinerator bottom ash (IBA) was also used for preparing 3DP-ECCs and showed a positive effect on the fresh properties of the material by decreasing the spreading diameter and the dynamic stress, while the plastic viscosity increased, indicating a better printability [129]. The pretreated IBA led to an increase in tensile strength by 7%, while the compressive strength decreased by 22%. The early-age shrinkage of 3DP-ECC was significantly decreased by adding pretreated IBA. The autogenous shrinkage at 7 days and the plastic shrinkage at 24 h were decreased by 56% and 30%, respectively. The substitution of IBA influenced the hydration products and pore structure of 3DP-ECC mainly at the early age: for example, the content of portlandite at 3 days and the content of calcium carbonate at 7 days were decreased by 30.9% and 29.9%, respectively. The volume fraction of macropores increased by approximately 300% and 500% at 3 days and 7 days, respectively, which caused a reduction in compressive strength as well as early-age shrinkage. Due to the lack of formworks, once printed, 3DP-ECC is directly exposed to the environment and undergoes a higher shrinkage compared to traditional concrete. Thus, IBA can mitigate the risk of cracking due to shrinkage, especially for on-site 3D printing applications in real environmental conditions [129].

4.5. Printing Parameters with ECCs

For printing, pumpable mixtures with the requirement of the highest bulk yield stress and extrudability (i.e., below the shear yield stress limit) should be preferred because they should result in excellent buildability [69]. Thus, the use of rheology-modifying agents is of paramount importance for the development of ECC composites with dough-like texture in the fresh state [69]. Among the influencing parameters, the liquid-to-solid ratio of the mix is highly pertinent to the shape stability of printable mixtures, rather than the superplasticizer content. The particle size distribution and the ratio of liquid to total surface area of all solids are also more pertinent than the addition of rheology-modifying agents. In addition, these agents do not significantly influence the mechanical properties of printed composites [69]. Mixtures with a 2 vol% of PVA fibers with a bulk yield stress of 34.26 kPa could pass through a 5 m hose in ref. [69].

In [119], the fresh ECC mix (20 min after water addition) with a w/b of 0.24 and 1.2 vol% of PVA fibers and an initial spread diameter of 132 mm was filled into a cone and showed, after cone removal, a spread diameter under a weight of 600 g equal to 106 mm. This mix was used to print a 1.5 m high twisted column with 150 printed layers of 10 mm.

For buildability measurements, a 10-layer structure was printed with a rectangular printing nozzle (10 × 100 mm^2) in [114]. Each layer was theoretically 10 mm in height (h_d) and 100 mm in width (w_d), and the real height (h_p) and width (w_p) of each printed layer were measured by means of a ruler and compared with the theoretical ones. Then, the relative deviation in height (d_h) and width (d_w) were calculated by means of Equations (8) and (9), respectively:

$$d_h(\%) = \frac{|h_d - h_p|}{h_d} \times 100 \quad (8)$$

$$d_w(\%) = \frac{|wh_d - w_p|}{w_d} \times 100 \quad (9)$$

The total height of the 10 printed layers was 99 mm, 98 mm, and 97 mm for mixes with 2.0%, 1.5%, and 1.0% PE fibers, respectively. The corresponding deviation value, d_h, was equal to 2% at maximum, while the deviation width, d_w, was no more than 6%. All the prepared mixes in [114] showed excellent buildability and shape-retention ability when printing 10 layers at a time.

A uniaxial unconfined compression test (UUCT), on a cylinder with a diameter of 70 mm and a height of 140 mm, was also proposed to evaluate the green compression strength of printable mortars in [71]. When the UUCT is performed at different time intervals after mixing, it can determine the initial yield strength and apparent Young's modulus as well as their evolution over time. Young's modulus appeared to be the critical fresh mechanical parameter for the two developed mixes and was equal to 209.3 kPa (mix A) and 54.6 kPa (mix B). Both mixes had high initial yield stress and presented no plastic failure during buildability tests.

Another way of assessing buildability was illustrated in [130]: a 24-layer structure with a height of 120 mm and a horizontal width of 28 mm was printed, and the slump ratio (β) of the total stacking height after 48 h of printing was calculated. When β was higher than 9%, the buildability was considered unacceptable, while if β was below 3%, the proposed lightweight ECC possessed ideal buildability and maintained stability without huge deformation during the printing process.

In [131], a six-axis robotic arm with an extruder and a nozzle of 5 × 30 mm^2 printed with a linear speed of 15 mm/s. The mix was made of 0.6 OPC, 0.3 FA, and 0.1 SF, the sand-to-binder ratio was 0.2, and the nanoclay-to-binder ratio was equal to 0.005, while the water-to-binder ratio was 0.3. Finally, a 1 vol% of PE fibers with a diameter of 24 μm and a length of 12 mm was added. The printing process was strictly controlled, and the distance between the nozzle and the printed layers was minimized to improve the interface between the layers as well as the quality of printing.

A mix made with 656 kg/m^3 of OPC 52.5, 118 kg/m^3 of SF, 604 kg/m^3 FA, 410 kg/m^3 of sand with a maximum size of 1.18 mm and a fineness of 1.62, 1.5 vol% of ultra-high-molecular-weight PE fibers, and a water-to-binder ratio of 0.26 was extruded through a 30 mm diameter nozzle and used as a formwork for casting concrete in [132]. The printed filament height was in the range from 10 to 30 mm, and the speed rate of the nozzle was 40 mm/s. The interfacial bond strength between the 3DP-ECC and cast concrete was influenced by the fiber content and filament printing height, showing an improvement and then a reduction. It was then also observed that there was a limited difference in the width of the interfacial transition zone between the printed and cast concrete when the filament printing height was 15 mm and 20 mm, while the width was reduced when the filament printing height was 10 mm. The same mix design and printing conditions were then used to investigate the interlayer bonding properties in [133]. Elliptical and flattened pores were observed within the interfaces, and their sphericity was influenced by the printing height of the filaments: a higher thickness increased the pore sphericity. When the fiber content was equal to 1.5 vol% and the printing filament height was 15 mm, the porosity at the interface was reduced. When the fiber content increased and the filament printing height rose, the interlayer interface bonding strength first increased and then decreased, evidencing the importance of an appropriate filament printing height and fiber volume content.

A mix based on 259.2 kg/m^3 of CEM I 42.5, 604.9 kg/m^3 of blast furnace slag, 864.1 kg/m^3 of limestone powder, 26 kg/m^3 of PVA fibers (2 vol%), 5.1 kg/m^3 of HPMC, 17.3 kg/m^3 of SP, and 345.6 kg/m^3 of water was printed in filaments that were 10 mm in thickness and 50 mm in width at 100 mm/s in [79]. The initial bulk and shear yield stress was equal to (34.74 ± 5.20) kPa and (4.41 ± 0.18) kPa, respectively. The time interval between two contiguous filaments was 3, 2, and 4.5 min, respectively, for samples

printed with two, three, and four layers. After 28 days of curing, a compressive strength of (44.09 ± 4.33) MPa was reached by the printed layers perpendicular to the load, while it was equal to (41.93 ± 1.88) MPa for the printed layers parallel to the load. Moreover, these average compressive strength values were close to that of cast samples. Extruding a filament against the previous one was a good strategy to increase its bond strength as well as to orient the fibers perpendicular to the printing direction.

To sum up, the key points related to the fresh mix properties are as follows:

- The order of mixing the products is fundamental in 3DP-ECC: First, solids are dry-mixed, then water and SP are added, and fibers are progressively introduced in the mix. Finally, the VMA is supplemented;
- The open time should be 30–60 min and should be compatible with buildability;
- An optimized particle size distribution guarantees a good packing of particles and contributes to buildability;
- The mix should have a low initial stiffness to be pumped and extruded, while the buildability requirement requires a stiff material able to bear its own weight;
- Fibers increase the yield stress at rest times, as well as the plastic viscosity and the dynamic yield stress;
- HPMC increases the viscosity and the thixotropy and prevents segregation when pumping as well as favors the internal curing effect;
- A high thixotropy is helpful to guarantee that the extruded layers firmly stack up;
- Microsilica, ground silica flour, and attapulgite nanoclay improve early strength and thixotropy and enhance cohesion. The silica fume content and the water-to-solid ratio are important parameters to optimize the fresh properties and strain-hardening behavior. Calcium aluminate and sulphoaluminate cements increase the early flowability and the early strength;
- The liquid-to-solid ratio of the mix is fundamental for the shape stability of printable mixtures, rather than the superplasticizer content;
- A nozzle with a smaller width-to-height ratio has a higher probability of smooth printing;
- The maximum printable height value can be estimated and used to set the nozzle standoff distance when printing to avoid structural instability problems;
- ECC pastes behave as non-Newtonian fluids, whose behavior is usually described by the Bingham model;
- The yield stress of the mix should be lower than the maximum shear force exerted by the extrusion system;
- The yield stress can be related to the slump value.

5. New Compositions

5.1. Use of Limestone-Calcined Clay Cement

Manufacturing ECC requires a high cement content because of the absence of coarse aggregates, contributing to high carbon emissions and energy consumption. Thus, more sustainable ECC compositions must be developed for the 3D printing process [52]. To this aim, limestone-calcined clay cement (LC3), a new cement based on limestone, calcined clay, and cement, appears to be a sustainable alternative to ordinary Portland cement (OPC) [134–136]. The tensile strain capacity of LC3-based ECC reached 6%, with an average residual crack width below 50 μm, and the compressive strength reached 32 MPa [137]. Lightweight engineered cementitious composites with LC3 cement (LL-ECC) and polyethylene (PE) fibers were studied in [52]. The optimal mixture for 3D printing due to rheological properties and suitable open time range was the LL-ECC with a 1.25% PE fiber content. Moreover, the compressive strength and fracture toughness of the printed LL-ECC-1.25% showed weak anisotropy. Additionally, the printed LL-ECC-1.25% evi-

denced a higher shear strength and energy dissipation ability with respect to mold-cast LL-ECC-1.25%. These results were attributed to the relatively high interlayer bond strength (2.62 ± 0.18) MPa, the fiber orientation, and the piling up of layers due to the printing procedure. Moreover, printed LL-ECC-1.25% beams presented 40% higher flexural strength than cast samples with close damage patterns and a limited anisotropy. The cracks in the printed beams were fully developed and spread throughout the section. A gantry-type 3D printer was used with an extrusion rate of 0.9 L/min and a nozzle travel speed of 30 mm/s. Finally, LL-ECC-1.25% was more sustainable than regular OPC-ECC: its embodied energy was equal to 3.952 MJ/kg, while the carbon footprint was 483 kg/m^3 [52].

On the contrary, in [138], the tensile strength and strain capacity of printed LC3-ECC decreased by 16.6–22.7% and 43.3–54.6%, respectively, compared to that of cast specimens. This was mainly due to a heterogeneous orientation of the PVA fibers during printing. The loss in strain capacity was more pronounced than that of the tensile strength, highlighting that the bridging ability of the fibers was decreased. Moreover, the compressive and flexural strengths presented significant anisotropy, which became more prominent at 28 days with respect to 7 days. Moreover, the x/y/z compressive strengths and y/z flexural strengths of the printed LC3-ECC were higher than those of the cast specimens. A lower flexural strength was noted in the x-direction and was attributed to the presence of the printed interfaces. SEM observations and X-CT scan images evidenced that the pore structure of the printed LC3-ECC was denser than that of the cast specimens. The number of pores bigger than 0.25 mm in the printed LC3-ECC was relatively lower than that of the cast specimen, but the pores in the printed samples were rather ellipsoidal, resulting in anisotropic properties of LC3-ECC. Compared to the mold-cast samples, 3DP improved either the compressive and the flexural strength of LC3-ECC, as well as its strain-hardening and multiple cracking behaviors. The 3D concrete printer head moved with a speed of 50 mm/s, and the extrusion rate was 1.5 L/min, while the nozzle had a diameter of 15 mm. The printed layers had a height of around 7.0–7.2 mm.

In [139], two ECC formulations, LC3-ECC and calcium sulphoaluminate–ECC (CSA-ECC), were designed to be printed and compared with cast materials. Cast LC3-ECC showed a gradual stabilization of shrinkage during the 28-day air-curing period, while CSA-ECC evidenced an expansion behavior either under air-curing or wet-curing conditions. Moreover, 3-day wet curing after demolding led to a consistent expansion of CSA-ECC. The experimental results highlighted that when keeping the same compositions and curing conditions compared with that of cast ECC, printed ECC had a greater shrinkage or a decreased expansion. The main reason was the exposition of the material to an external environment at an early stage. On the contrary, wet curing or water spraying during the first hours after printing CSA-ECC led to an expansion of the material. Considering the important expansion observed in cast CSA-ECC, the increase in the wet-curing time after printing guaranteed a certain expansion. The designed LC3-ECC and CSA-ECC materials had a much lower carbon footprint (by 75% and 59%, respectively) than the concrete reference and lower embodied energy than classic M45-ECC (by 73% and 67%, respectively; M45-ECC had a tensile strength of 4.5 MPa and a strain capacity of 3% at 28 days). In addition, when taking into consideration the higher mechanical properties of ECCs to reduce the size of the structure with the aim of reducing material consumption, the embodied carbon and energy in printed ECC structures will be significantly reduced with respect to that of concrete structures. The mechanical properties of printed ECC surpassed those of cast specimens, and printed CSA-ECC samples demonstrated similar or even higher mechanical properties than printed LC3-ECC. However, when carbonation was actuated, the flexural performance of printed ECCs decreased. Thus, carbonation curing used to mitigate the carbon footprint of materials should be performed with care.

Moreover, the open time of a fresh mixture can change when using different printing setups, requiring the adjustment of the proportion (or CSA dosage) to satisfy specific printability requirements. Finally, the impact of a prolonged wet-curing time on the expansion behavior of CSA-ECC requires further investigation [139]. A rectangular nozzle was mounted on a six-axis robotic arm which moved at 3 m/min. The layers were 10 mm in height and 30 mm in width.

5.2. Strain-Sensing Cements

Recently, functionalized cementitious materials with strain-sensing ability were also 3D-printed [140]. The cementitious materials were made by adding graphite (G), milled carbon microfibers (MCMFs), and/or chopped carbon microfibers (CCMFs) to reach electrical percolation and activate a piezoresistive effect. The results showed that electrical percolation was reached by using a mix of G and CMFs. In particular, with respect to the weight-to-cement percentage (wt%), optimal mixtures were obtained when adding 10 wt% G and 0.5 wt% MCMF for G+MCMF specimens, 10 wt% G and 0.125 wt% CCMF for G+CCMF specimens, and 10 wt% G, 0.250 wt% MCMF, and 0.125 wt% CCMF for hybrid filled G+MCMF+CCMF specimens. The 10G250M125CCMF mixture (10 wt% G, 0.25 wt% MCMF and 0.125 wt% CCMF) demonstrated optimal sensing performance and mechanical strength. Specifically, a static gauge factor of 622, a resolution of 167 με, an accuracy of 19.24 με, and a Young's modulus of 798 MPa were measured [140]. The gauge factor is the ratio of the relative change in resistance divided by the strain.

5.3. Rubberized ECCs

In recent times, rubberized ECCs were proposed in [141]. All the compositions investigated reached a compressive strength of 25 MPa, required for structural applications, except for the one with 15% rubber. Rubberized ECC containing 5% waste crumb rubber (CR) was 3D-printed and showed strong anisotropy, highly evident during flexural tests. Testing in parallel to the fiber direction resulted in 3 and 4% higher early-age and lateral compressive strengths, respectively, compared to the z direction, perpendicular to the fiber direction. In addition, the printed specimens showed less stiffness, more deflection capacity, a prolonged strain-hardening region, higher peak stress, and higher post-peak stress compared to the mold-cast ones. Moreover, flexural tests revealed that when loaded according to the z direction, where the fibers were parallel to the longitudinal axis of the printed sample, increases of 104% and 47% in the 7- and 28-day flexural strengths, respectively, were evidenced with respect to the specimen printed in the z' direction, where the fibers were mostly perpendicular to the longitudinal axis of the printed specimen. This could be due to the ability of the fibers to resist tensile stresses parallel to the longitudinal axis of the sample when undergoing flexural tests, along their length. Compared to the mold-cast specimen, 158% and 75% higher 28-day flexural strengths were noted for the printed specimens in the z and z' directions, respectively, which were due to the alignment of the fibers during the extrusion from the nozzle and to their uniform distribution within the specimens. In addition, the samples printed in the direction parallel to the fiber orientation revealed 27% less drying shrinkage compared to the perpendicular direction after 56 days of printing. Finally, shrinkage strains decreased by 64% and 74% for the perpendicular and parallel printing directions, respectively, when compared to the mold-casted samples. The reasons were a higher number of voids due to the CR aggregates and the presence of weak joints between printed layers that could block water [141]. The samples were printed with a HC1008 Desktop Concrete 3D Printer and a 20 mm nozzle.

5.4. Carbonation Curing

Carbonation curing was proposed with ECCs to reduce their carbon emissions. This process has the advantage of rapidly leading to high-strength cementitious products when carried out at an early age. In addition to cement, alkaline industrial by-products rich in Ca^{2+}, Al^{3+}, Mg^{2+}, etc., can be carbonated if present in the mix and contribute to the formation of stable carbonates that improve the fiber–matrix interface and the mechanical properties of ECCs [142]. However, the CO_2 concentration (20%) and pressure need to be high, which limits the use of this technique to prefabrication plants.

Carbonation curing was also associated with the use of sisal fibers in [44]. The selection of sisal fiber for low-carbon ECC manufacturing targeted several purposes. First, from a sustainability point of view, sisal fiber increased carbon sequestration by 10% by favoring diffusion transport of CO_2 into the samples during carbonation curing due to their hollow structure. Then, from a mechanical performance point of view, sisal fibers enhanced the tensile ductility of the ECC by acting as artificial flaws and triggering a larger number of microcracks in the matrix during tensile strain hardening. The cast specimens were demolded 18 h after manufacturing and dried with a fan for 4 h to remove water from capillary pores and enhance CO_2 diffusion. Then, the samples were cured for 24 h under 5 bars of CO_2 (99.8%purity) at room temperature (23 $\pm$ 2) °C. The addition of 0.5% sisal fibers led to an ultimate tensile strength of (6.14 $\pm$ 0.02) MPa with an ultimate tensile strain of (8.62 $\pm$ 1.28)% after carbonation curing. The lowered alkalinity due to carbonation curing is also expected to mitigate the well-known degradation problem of sisal fiber in cementitious composites [44].

To sum up, the following are observed:

- More sustainable ECC compositions based on limestone-calcined clay cement (LC3) can be successfully developed and printed;
- New mixes containing crumb rubber, recycled aggregates [118], and conducting fillers can be printed to produce more sustainable and self-sensing concretes;
- Carbon curing can be actuated on ECCs, which can lower the pH of the matrix and make it more compatible with natural fibers.

6. Mechanical Properties and Durability of Printed ECCs

6.1. Anisotropy of Mechanical Properties

Several papers [20–22] evidenced that the mechanical strength of the interfaces between deposited layers is significantly influenced by the material composition, print time interval, surface moisture, and physical layer interlock, as well as extrusion speed. However, no systematic characterization of interface toughness has ever been performed. These interfaces may also influence the compressive strength, resulting in anisotropic compressive strength and different stress–strain relationships in the parallel and perpendicular directions to the printing direction. While anisotropic compressive strength [23–25] is well known, the constitutive stress–strain laws in the longitudinal and transverse directions necessary for the structural design of 3DP-ECC elements have not yet been investigated [119].

Printed ECCs show anisotropic properties, maintaining the tensile strain-hardening features in the printed filaments according to the printing direction, while the ductility in the filament in the perpendicular directions is much lower, specifically in the vertical direction across the interfaces. This anisotropic behavior is not surprising due to the fiber alignment in the printing direction during the extrusion process, although the magnitude of fiber alignment depends on various printing parameters. Surprisingly, a minimal toughness across the interface between superposed filaments is observed, probably due to fibers crossing the filaments when printed layers are deposited while still in the fresh state. The weaker interfaces between printed filaments remain a bottleneck that needs further efforts

by researchers to ensure structural reliability and robustness for full-scale structures. Other research areas should be studied as well, like, for example, the curing of printed structures, long-term durability under various environmental exposures, and the response to different loading types (static, impact, creep, etc.). In addition, the quantitative determination of fiber distribution and orientation due to the extrusion step and the way these have to be incorporated into mechanical models appear also as a major research topic priority. Once these studies are completed and validated by large-scale structural tests, the emergence of 3DP-ECC structures will be possible [13].

The mechanical anisotropy coefficient (I_a) can be calculated according to Equation (10), as proposed in [142]:

$$I_a = \frac{\sqrt{(f_x - f_c)^2 + (f_y - f_c)^2 + (f_z - f_c)^2}}{f_c} \quad (10)$$

where, f_x, f_y, f_z are the compressive, tensile, and bending strengths, etc., of printed materials tested in the x, y, and z directions, respectively. f_c is the strength of mold-cast samples. For cast samples, considered as homogeneous materials, $I_a = 0$.

In [119], as expected, an increase in the compressive strengths of 3DP-ECC samples with curing ages from 1 day to 28 days was observed, as well as anisotropic behavior. The specimen cut perpendicular to the printing direction (Prism-Per) had a more ductile failure mode together with a higher compressive strength and strain and a gentler descending branch compared to those cut parallel to the printing direction (Prism-Par) specimen. However, due to the closing of the space at layer interfaces, the elastic modulus of the Prism-Per specimen was 16% lower than that of the Prism-Par one, which could potentially induce a larger deformation of the 3DP-ECC element and needs a special attention in the design of 3DP structural elements. Under uniaxial tensile load, the 3DP-ECC showed multiple microcracking and strain-hardening performance, with a strain capacity of 3.0%. For printed samples with a smooth interface, a fiber-bridging effect was noted in broken samples, contributing to a limited increase in the load–displacement curve after an initial decrease, when a crack grows along with the interface from the notch tip. This effect was due to fiber interpenetration across the deposited filaments while in the green state. However, the interface remained quasi-brittle. To overcome this drawback, grooved layers were printed by means of a shaped nozzle (groove depth and width were about 3×3 mm^2). Then, mechanical interlocking between the deposited filaments was observed, and this led to a non-brittle failure response associated with a higher loading capacity. Groove printing seems to be a promising solution to produce tougher filament-to-filament interfaces and limit the delamination failure tendency of 3DP-ECC structures [119]. A six-axis robotic arm with a pump installed on a linear gantry was used to print the samples. The nozzle had a cross-section of 30×10 mm^2, and the printing speed was 50 mm/s (extrusion speed equal to 0.9 L/min).

6.2. Patterned Structures

The flexibility and precision of the 3D printing technique were fully exploited to design personalized and customized structures able to mimic complex biological structures with high performance in [143] (Figure 7). Then, investigations on the fracture behavior of 3DP-ECC with Bouligand structures replicating a mantis shrimp shell were conducted.

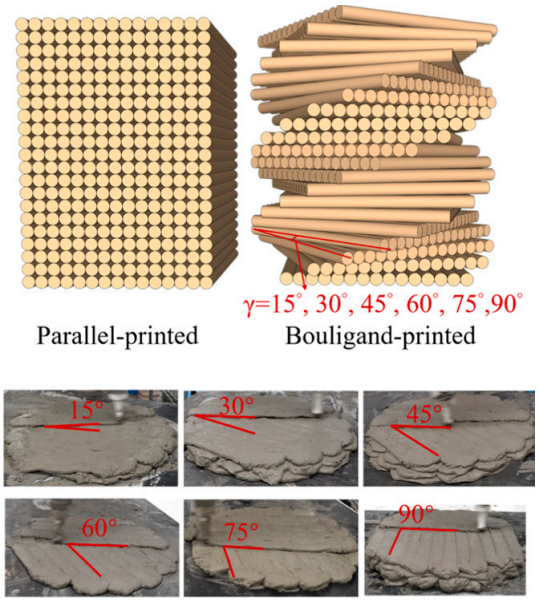

Figure 7. Parallel- and Bouligand-printed structures with different pitch angles (γ). Reproduced from ref. [143]; published by Elsevier, 2025.

Three groups of samples, including parallel-printed, Bouligand-printed, and mold-cast notched beam specimens, were manufactured and tested in three-point bending. A six-axis robotic arm alimented with a pump was used with a rectangular nozzle (3×50 mm^2). The flow rate was set to 0.02 L/s, while the nozzle travel speed was 100 mm/s. The influence of different pitch angles (15°, 30°, 45°, 60°, 75°, and 90°) on the fracture behavior of the 3DP-ECC specimens was studied too. The parallel-printed specimens presented a more uniform and brittle failure mode, while the Bouligand-printed samples showed different fracture patterns, characterized by microcracking, crack delamination, crack branching, crack bridging, and crack twisting. Contrarily, the cast samples evidenced a singular, almost linear crack propagation path with microcracking and fiber bridging. The parallel-printed specimens evidenced a flexural strength and fracture energy of 33% and 67% lower than those of the cast samples, respectively, while the Bouligand-printed specimens showed a flexural strength ranging from 0.97 to 1.29 times and a fracture energy ranging from 0.99 to 1.63 times that of cast specimens. The Bouligand-printed samples with a 30° pitch angle gave the highest values. The parallel-printed specimens presented a fracture toughness 60% lower than that of the cast specimens. On the contrary, the Bouligand-printed samples showed a toughness ranging from 2.24 to 3.76 times that of the parallel-printed specimens and 0.87 to 1.47 times that of the cast specimens, with, again, the highest toughness for a 30° pitch angle. Finally, the fracture behavior of 3DP-ECC with Bouligand structures was simulated by means of a combination of the concrete plastic damage model and cohesive elements. The simulation results were in good accordance with the experimental data, with errors ranging from 1.45% to 7.16%. Cohesive elements underwent shear and tensile failure, which was consistent with experimental observations. The synergistic effects of crack twisting and bridging in the Bouligand-printed samples were able to enhance the toughness, in agreement with natural toughening mechanisms. A 30° pitch angle provided optimal energy absorption, maximizing the crack bridging and twisting effects and resistance to crack propagation. A nonlinear regression analysis method was also used to model the relationships between pitch angles, flexural strength, fracture energy, and toughness. The maximum flexural strength was obtained with a pitch angle of 31.44°, while the highest fracture toughness occurred at 30°, and the maximum fracture energy was reached for a pitch angle equal to 23.56°. These results evidenced that

the optimization of the pitch angle of 3DP-ECC with Bouligand structures could improve fracture performance for specific applications [143].

Knitted and tilted filaments were also designed to mimic the crossed-lamellar microstructure of conch shells and were printed in [144] (Figure 8). Their features were compared with filaments classically printed parallel each other. The fresh mix was put into a hopper connected to a peristaltic pump and transported through a 5 m long tube to a six-axis robotic arm.

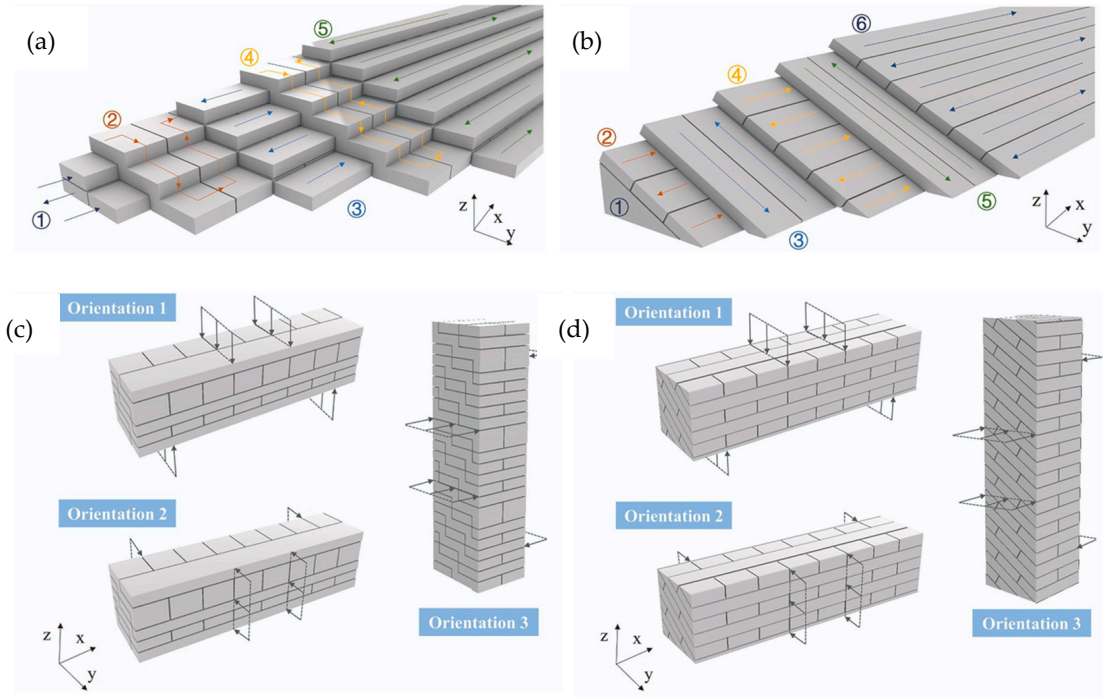

Figure 8. Schematic diagrams of filaments: knitted (**a**) and tilted (**b**); loading modes for filaments: knitted (**c**) and tilted (**d**). Arrows indicate loading directions. Reproduced from ref. [144]; published by Elsevier, 2023.

These patterns introduced a complex 3D interface system exploiting the original weak interfaces as a structural strengthening method. In four-point bending tests, parallel printed filaments loaded perpendicularly and parallel to the printing direction evidenced excellent flexural strengths and strain-hardening behavior, significantly higher than the cast specimens. These results were explained based on the fiber alignment in the extruded ECC filaments, the crack branching and deflection in the laminate structure, and crack trapping by the fibers. Knitted and tilted filaments had a bending strength higher than or comparable to cast ECC samples when tested according to orientations 1 and 2. Moreover, knitting and tilting filaments led to a unique failure mode: multiple cracks occurred from the bottom of the samples (tensioned zone) and rose in the loading direction. Further deflection and bifurcation then happened when the cracks met the filament interfaces, causing energy dissipation and delaying failure to increase ductility. Thus, anisotropy was notably reduced due to these innovative printing patterns. Moreover, when the specimens were tested according to orientation 3, a strong increase in flexural strength was noted in knitted and tilted filaments compared to parallel ones. An increase of up to 179% was measured in the tilted filaments, and the strength of the knitted filaments also increased compared to that of parallel filaments by 116%. The ratio of the strength in orientation 3 relative to orientation 1 was enhanced from 8.6% to 30%, indicating a notable reduction in anisotropy in 3DP-ECC.

Finally, without steel reinforcement in 3DP-ECC, durability concerns due to steel corrosion should be null. However, because of complex interfaces between the printed filaments, further research should be carried out to study the ingress and diffusion transport mechanisms of aggressive agents inside 3DP-ECC in harsh environments and the eventual damages to fibers and the matrix [144].

Table 2 reports the results of the best mixes reported in literature.

Table 2. Comparative results on 3DP-ECC.

Composition (In kg/m^3 If No Other Information)	Additives SP	w/b	Fiber Type and Content	Open Time Window	Slump/Thixotropy Index	Mechanical Strength	Ref.
259.2 CEM I 42.5, 604.9 BFS, 864.1 limestone powder, 26 PVA	5.1 kg/m^3 methylcellulose (201,000 mPa.s), 17.3 g/m^3 SP (BASF Glenium 51)	0.41	PVA 2 vol%	n.d.	Mixture could pass through a 5 m hose	6-10 MPa peak flexural strength // to printing direction ≈2–3 MPa tensile strength	[69]
480.2 CEM I 42.5, 567.6 FA, 109.1 limestone powder, 186.3 sand (125–250 µm), 294 sand (250–500 µm), 26 PVA	6.5 kg/m^3 methylcellulose (201,000 mPa.s,) 13 g/m^3 SP (BASF Glenium 51)	0.31	PVA 2 vol%	n.d.	Mixture could pass through a 5 m hose	≈1.6–3.1 MPa peak tensile strength	[69]
309 CEM I 52.5R, 1026 FA, 345 sand (50–550 µm), 26 PVA	2 kg/m^3 HPMC 7500–14,000 mPa.s (2% aqueous solution at 20 °C), 3 kg/m^3 SP polycarboxylate-based	0.24	PVA with 1.2% oil (by mass) 39 µm in ∅	70 min	Spread diameter from ≈132 to 123 mm after 20 and 60 min, respectively, in the flow table test. The mixture did not flow before the flow table drop was applied	31.2 MPa 28 d compressive strength //, 30.6 MPa ⊥ to printing direction on cubes (3.38 ± 0.03) MPa peak stress 28 d tensile stress with (3.09 ± 0.25)% strain capacity	[119]
656 CEM I 52.5, 118 FA, 246 SF, 604 sand, 57,120 mesh crumb rubber	3 kg/m^3 SP	0.27	1–2% PE 25 µm in ∅	n.d.	Spread diameter of 162 mm with 1.5% of fibers	19.4 MPa flexural strength with 1.5% fiber // to printing direction and 22 MPa ⊥ to printing direction	[114]
0.38 CEM II 52.5, 0.05 SAC, 0.09 SF, 0.48 FA, 0.26 sand * (<300 µm),	0.0004 HPMC * (viscosity of 38,000–42,000 mPa.s), 0.01 SP * polycarboxylate-based	0.26 water *	0.018 PE * 24 µm in ∅	n.d.	n.d.	62.8 kN peak load four-point bending test // to printing direction and 32.3 kN ⊥ to printing direction on 500 mm long and 100 mm high beams	[145]
0.4 CEM II 52.5, 0.03 SAC, 0.57 FA, 0.4 sand	0.001 HPMC°, 0.005 ANC°, 0.012 SP°	0.28 water°	1.5 PE° 24 µm in ∅	n.d.	Slump flow = 55 mm and spread flow = 155 mm; shear thinning behavior and dynamic yield stress of ≈550 Pa; and plastic viscosity of ≈11.7 Pa.s with 2% of PE fibers	(5.68 ± 0.4) MPa ultimate tensile strength with (9.57 ± 1.01)% tensile strain capacity	[78]
0.38 CEM II 52.5, 0.05 SAC, 0.09 SF, 0.48 FA, 0.26 sand	0.0004 HPMC (viscosity of 38,000–42,000 mPa s), 0.001 SP polycarboxylate-based	0.26 water	0.018 PE 24 µm in ∅	n.d.	n.d.	(6.15 ± 0.15) MPa ultimate tensile strength with (7.31 ± 1.83)% tensile strain capacity	[73]
72 CEM I, 23 FA, 5 CAC, 45 sand, 10 MS, 5 GS, 5 ANC,	0.4 HPMC¨, 0.8 SP¨	43 water¨ (w/b = 0.36)	2 vol% PVA	n.d.	n.d.	≈6 MPa tensile strength with ≈4% tensile strain capacity	[68]

Table 2. *Cont.*

Composition (In kg/m^3 If No Other Information)	Additives SP	w/b	Fiber Type and Content	Open Time Window	Slump/Thixotropy Index	Mechanical Strength	Ref.
483 CEM 42.5, 314 BFS, 70 SF, 447 LS powder (<250 µm), 284 sand (125–250 µm),	5.2 HPMC (Tylose MHS 15002 P6), 3.47 SP		26 PVA 40 µm in ∅	3 h 30 min, determined by Vicat penetration test	n.d.	(8.68 ± 2.00) MPa maximum flexural strength	[71]
1 OPC, 0.11 SF, 0.89 sand, 0.8 hollow glass microspheres (20 µm in ∅)	0.015 SP¨	0.65 water¨ (w/b = 0.59)	0.0175 PVA¨ 39 µm in ∅	n.d.	153 mm slump flow 65 min setting time	(8.46 ± 0.39) MPa flexural strength // to printing direction and 9.12 ± 0.30 MPa ⊥ to printing direction at 28 days	[130]
656 CEM I 52.5, 118 SF, 410 sand	2 SP	363 water (w/b = 0.47)	15 PE 24 µm in ∅ (1.5 vol%)	n.d.	≈167 mm initial spreading diameter, ≈154 mm spreading time after 100 min	7.51 MPa maximum flexural strength with a strain capacity of 5.4%	[146]
730.41 OPC 52.5, 87.65 SAC, 233.73 FA, 116.87 SF, 701.19 sand (330 µm average diameter)	0.18 HPMC, 23.4 SP	257.1 water (w/b = 0.22)	17.53 PVA 40 µm in ∅	Open time of ≈40 min	Initial setting = 37 min, final setting time = 64 min, determined by isothermal calorimetry, dynamic yield stress of 2505 Pa and plastic viscosity of 140.2 Pa.s with 2% of PE fibers	1.43 kPa initial compressive strength, with a stress increase rate of 0.095 kPa/min.	[147]
1 CEM I 52.5, 1.26 FA, 0.11 densified SF, 5 vol% to FA waste aggregates (1–2 mm), 0.89 sand (<600 µm)	6 mL SP polyether-based superplasticizer	0.65 water (w/b = 0.41)	1.75 vol% PVA 39 µm in ∅	n.d.	240 mm slump diameter	≈9.3 MPa flexural strength // to printing direction, ≈6.2 MPa flexural strength ⊥ to printing direction at 28 days	[141]
0.47 OPC 42.5R, 0.44 FA, 0.09 FA, 0.29 sand	0.0018 SP	0.24 water	0.01 PE 24 µm in ∅	n.d.	≈136 mm spread diameter and ≈25 mm slump 20 min after water addition, ≈127 mm spread diameter and ≈21 mm slump 80 min after water addition	≈7 MPa peak tensile strength with ≈4% tensile strain capacity	[72]
1 OPC 52.5, 1.33 FA, 0.11 SF, 0.89 sand	0.024 activated carbon powder, 0.025 VMA, 0.068 SP	0.65 water	0.021 PVA 39 µm in ∅	n.d.	n.d.	10.81 MPa // to printing direction, 10.08 MPa flexural strength ⊥ to printing direction at 28 days	[148]
0.6 OPC, 0.3 FA, 0.1 MS, 0.2 sand	0–0.5% nanoclay	0.325–0.375 w/b, function of fiber content	1–2 vol% PE 24 µm in ∅	n.d.	Slump = 10.5 mm and slump flow = 198 mm for mix with 1 vol% of 12 mm in length fiber and w/b = 0.35, Static yield stress = 530.8, 809.1, 1477.3, 2552.7, and 3870.1 Pa for 0, 0.5, 1.0, 1.5, and 2.0 vol% of fibers, respectively	n.d.	[53]
75 wt% CEM II/A-M (S-LL) 52.5R, 15 wt% SF and 10 wt% FA	none	0.22–0.24 w/b	0.3–1.5 vol% HDPE 12 µm in ∅	n.d.	119 mm spread diameter and 133 mm after shocks (w/b = 0.22, s/b = 0.2 and 1.5 vol% fibers)	5.66 MPa tensile strength with 3.21% ultimate tensile strain (w/b = 0.22, s/b = 0.2, and 1.5 vol% fibers)	[70]

Table 2. *Cont.*

Composition (In kg/m^3 If No Other Information)	Additives SP	w/b	Fiber Type and Content	Open Time Window	Slump/Thixotropy Index	Mechanical Strength	Ref.
360 OPC 52.5 R, 196.5 MK, 98.3 LS, 360.3 GGBFS,	1.0 HPMC, 4.0 SP	264 water	10–17.5 kg/m^3 PE fibers 24 µm in ∅	5–45 min recommended	Initial slump diameter of 115 mm and of ≈103 mm after 60 min, initial flow diameter of 130 mm and of ≈115 mm, flow table test (1.25 vol% of fibers)	Anisotropic parameter = 0.799 on nominal flexural strength and 0.067 on compressive strength (1.25 vol% of fibers)	[119]
223 PLC, 71 MK, 51 LS, 841 FA, 30 SF, 30 CR (40–80 mesh), 466 sand	4.0 SP	253 water	26 PVA 39 µm in ∅	60 min	Spread diameter = 165 mm 20 min after water addition, ≈145 mm 60 min after water addition	≈4.8 MPa tensile strength with ≈2.7% tensile strain capacity	[52]
0.6 OPC, 0.3 FA, 0.1 SF, 0.2 sand (100–300 µm)	0.005 nanoclay	0.3 water	1 vol% UHMWPE fibers 24 µm in ∅	n.d.	n.d.	17.41 MPa flexural strength Bouligand structure at 30° in the z direction	[143]
497 OPC, 781 FA, 332 sand	2.5 SP	320 water (w/b = 0.25)	26 PVA 39 µm in ∅ (2 vol%)	n.d.	n.d.	21.6 MPa flexural strength // to printing direction, ≈16.5 MPa ⊥ to printing direction	[144]

(n.d.: not determined, SP: superplasticizer, SAC: sulphoaluminate cement, *: mass ratios of the binder mass (CEM+SAC+FA+SF), °: mass ratios of the binder (OPC+SAC+FA) weight, except the fiber content (volume fraction), ANC: attapulgite nanoclay, CAC: calcium aluminate cement, LS: limestone, MS: microsilica, GS: ground silica, ¨: % to total cementitious materials, BFS: blast furnace slag, VMA: viscosity-modifying agent, HDPE: high-density polyethylene, MK: metakaolin, SG: semi-hydrated gypsum, GGBFS: ground granulated blast furnace slag, PLC: Portland limestone cement, CR: crumb rubber, UHMWPE: ultra-high-molecular-weight polyethylene).

To summarize:

- 3DP-ECCs show anisotropic properties according to the printing direction;
- The ductility in the filament in the perpendicular direction is much lower, specifically in the vertical direction across the interfaces;
- Groove printing seems to be a promising solution to produce tougher filament-to-filament interfaces;
- Patterned structures like Bouligand ones, as well as knitted and tilted structures, can improve fracture performance for specific applications. They also fully exploit 3D printing potentialities;
- Durability aspects of 3DP-ECCs are still to be investigated.

7. Critical Steps in the Printing Process

In [72], cast specimens performed better than printed ECCs in terms of multiple cracking ability, tensile strength, and strain capacity. In fact, both the fibers and cementitious matrix were responsible for the performance decrease when printing. When the blades of the pump rotated, fresh ECC was continuously submitted to shear stress in the hopper and extruded out of the nozzle in a twisted form. As a result, the thin synthetic fibers were curled because of their flexibility. This curling effect then hampered the crack-bridging ability of the fibers, which were not totally exploited under tension. In addition, the orientation of the fibers inside the twisted filament was rather well aligned with the printing direction, while fibers in the cast specimens presented a random distribution and orientation. For example, in the filaments printed with a nozzle standoff distance of 12 mm and a speed of 8 m/min, a fiber orientation of about 45° with respect to the printing direction was noted and weakened the tensile resistance in the printing direction. Moreover, in the samples printed with a nozzle standoff distance of 12 mm and a speed of 7 m/min, the fibers were oriented almost perpendicular to the printing direction and led to

a limited tensile strength with a low printing speed. It was also expected that the extrusion step guaranteed less porous specimens than cast ones because the shear forces made the material denser [70,149]. However, this was not always what happened; in fact, cast ECCs could have a higher volume of finer pores compared with 3DP-ECCs. Thus, cast ECCs presented a higher initial cracking strength under tensile loads because of a denser matrix. The standoff distance of the nozzle strongly influenced the tensile strength of 3DP-ECC: a lower standoff distance led to a higher mechanical performance. For a lower standoff distance, the nozzle flattened the fibers and better aligned them in the horizontal plane because of an extra compressive stress. Consequently, the out-of-plane angle of the fiber was limited, and the tensile resistance in the printing direction was higher due to better fiber orientation. At the same time, as the material compacted after deposition, due to the action of the nozzle, the pore structure was slightly impacted. Thus, lower standoff distances produced a less porous matrix, and the initial cracking stress of the 3DP-ECC was in general inversely proportional to the nozzle standoff distance. For example, when the nozzle standoff distance decreased from 14 mm to 10 mm, the strain capacity of the same mixture increased by about 30%, while the tensile strength was up to 39% higher. Concerning the nozzle travelling speed, moderate printing speeds yielded superior tensile strength, demonstrating that the printing speed may be optimized to lead to optimal tensile performances. However, low printing speeds could lead to potential accumulation of an excess of material: because of a limited space for the already printed material, the newly extruded one compressed the previously deposited one, yielding more aligned fibers perpendicular to the printing direction. For high printing speeds, though the matrix was compact, the tensile strength was lower because the extruded filaments were thinner than standard ones due to the reduced material volume flow. Therefore, a gentle smaller vertical secondary compaction was caused by the additional stress of the nozzle. Consequently, a higher number of out-of-plane fibers were produced, leading to a reduction in tensile strength [72].

The interfacial bonding between 3DP-ECC filaments has two origins. On one hand, part of the adhesion is due to the contact area between the fresh materials deposited and is related to the printing job. Then, the printing speed has a notable influence on the formation of weak interfaces. On the other hand, another contribution to interfacial bonding derives from fibers bridging the interface. As previously mentioned, when an upper layer of material is printed, its own weight presses it onto the underlying layer and part of the fibers penetrate in it, contributing to inter-layer fracture resistance. During flexural tests, the load first linearly increases as a function of the displacement until the fracture toughness of the matrix is reached. Then, the brittle fracture of the matrix leads to a rapid post-peak decrease in load without reaching the null value, as in the case of brittle failure of common cementitious materials. This is due to the presence of fibers that redistribute stress after matrix cracking and fibers bridging cracks that play a fundamental role in load bearing. The load capacity increases halfway until it reaches another peak or a plateau and allows for further development of a large deflection. The second rising branch characterizes the fiber bridging capacity of ECCs, and the enhancement in overall fracture resistance ability is notable [72].

Fibers are mainly responsible for the difference in fracture resistance between inter- and intra-layer specimens: fiber bridging capacity in printed layers is usually higher because of the fiber amount. Consequently, the fracture resistance of intra-layer specimens is much higher than that of inter-layer ones. Pore distribution along the layer stacking direction was studied by μ-computer tomography scanning, and it appeared that the inter-layer porosity area did not show significant differences from intra-layer ones. More pores were introduced into the bulk of the filaments than the interface due to the agitation of the pump.

Nonetheless, the pore distribution investigation also confirmed that a nozzle standoff distance slightly lower than the filament height could effectively eliminate the formation of interlayer voids [150]. To sum up, both the inter-layer and intra-layer fracture resistance capacity are proportional to the nozzle standoff distance due to the number of fibers bridging adjacent layers as a result of the deformation of the overlapping areas in contact. A higher nozzle standoff distance generally produced more important cross-sectional deformation. In addition, because of the unavoidable weight loading from the upper layers, the printed filaments are vertically squeezed, and the contact area of adjacent layers is augmented. In the meantime, the fibers close to the surface penetrate the cementitious matrix of the filament below, raising the interfacial fracture resistance. Interlayer bonding is then increased. Contrarily, a lower nozzle standoff distance produces less rounded cross-sections during extrusion, and the deformation between two successive layers is limited. Moreover, more fibers are flattened and aligned along the printing direction, reducing the number of fibers penetrating the interface and leading to weaker interfacial fracture resistance [72].

To sum up, the following observations are made:

- When the nozzle standoff distance decreases by about 30%, the strain capacity of the same mixture can be increased by about 30%, while the tensile strength can be up to 39% higher;
- Moderate printing speeds yield superior tensile strength;
- Low printing speeds could lead to potential accumulation of an excess of material and should be adapted to the feeding rate of the nozzle (better integration and interface between the hardware of the printing chain).

8. Current Technical Challenges and Limitations

Contrarily to what happens with conventional concretes, ECCs are designed and processed according to micromechanical principles [151,152] to trigger steady-state crack propagation and multiple cracking behavior [153–155]. However, as previously seen, manufacturing of these materials introduces variations in their properties, specifically in the case of a non-uniform fiber distribution within the cementitious matrix [13,76,156]. A loose fiber dispersion decreases fiber bridging abilities, potentially hampering the composite's strain-hardening capacity while also limiting tensile strength and strain capacity [157–159]. Thus, the rheological properties of ECCs in 3DPC must guarantee optimal fiber dispersion and suitable printability. This complexity shows that the rheological optimization of 3DP-ECC is much more difficult than in traditional 3D concrete printing as well as in casting common ECC mixes [121]. Thus, an innovative printability evaluation method specifically designed for 3DP-ECC that considers the impact of fiber dispersion while also emphasizing cost-effectiveness and efficiency was proposed in [121]. The method simplifies rheological parameters through slump and slump flow tests. Moreover, the determination of the printable open time is also possible, thus adjusting the mixing time of the ECC paste. The feasibility of the proposed method was validated through printing and rheological tests (the Marsh cone flow test was used as a fiber dispersion evaluation technique, and a flow time of between 24 and 33 s was set). The experimental results were in good agreement with theoretical ones. Finally, the tensile strength of 3DP-ECC was also studied, further validating this new methodology [121].

However, significant gaps in the field of 3DP-ECC structures need to be investigated deeper. Some of the parameters to take into consideration include the curing conditions of printed structures, their durability over time when exposed to different environmental conditions, and their response to diverse loads [13].

Internal curing can be actuated by means of lightweight aggregates like presoaked pumice [74]. A mix was made of 50% OPC and 50% GGBFS, 0.7 river sand, 0.01% methylcellulose, 0.0015% SP, 2 vol% of PE fibers that were 17.9 μm in ∅ and 6 (1 vol%)–10 (1 vol%) mm in length, and a water-to-binder ratio of 0.3. The flow diameter of ECC mixes with 2% PE fibers ranged from 14 to 15 cm. A printing speed of 1 cm/s with an extrusion rate of 0.1 rounds/s led to a smooth filament texture, dimensional consistency, and a stable extrusion process. The use of presoaked pumice aggregates caused a slight reduction in buildability (which was 16 layers with 30% of pumice aggregates). Other self-curing or internal curing agents could include polyethylene glycol (PEG) [160] or coarse biochar [161]. To the best of the author's knowledge, none of these have been used yet during ECC printing. Finally, fine biochar (10–20 wt% additions) has not only the potential to decrease the carbon footprint of cement in general but also to reduce the chemical and frictional bond strength between the fiber and matrix [162].

Possible methods to increase the tensile strength of printed ECCs include limiting the adverse impact of the progressive cavity pump and/or increasing the favorable wall effect of the extrusion nozzle. Future studies should also consider the evaluation of the fiber distribution and orientation in extruded filaments [119]. However, it should be emphasized that an extensive design based on micromechanics and fracture mechanics concepts is still needed to correctly understand the mechanical and electrical features of ECCs [163].

Moreover, due to the use of plastic microfibers, some concerns can be raised in terms of workers exposed during the preparation of the mixes as well as during the demolition of ECC structures. Cerebral and epithelial human cells exposed to 3–16 μm PE fibers under 10 ng/mL–10 μg/L for 24–48 h during in vitro tests showed oxidative-stress-induced cytotoxicity [164]. Thus, personal protection equipment (gloves, googles, and respiratory masks) is recommended when handling them. On the contrary, electrospun PVA nanofibers are used in tissue engineering and scaffold production because of their biocompatibility and biodegradability [165].

To summarize, the following observations are made:

- Fiber dispersion is of paramount importance, and rheological properties should be adapted;
- Internal curing should be considered to improve mechanical strength;
- Further micromechanics and fracture mechanics concepts should be studied to understand the mechanical behavior of 3DP-ECCs;
- Safety precautions should be taken by workers when handling PE fibers.

9. Advancing the Field of ECCs Through Machine Learning

In the last years, machine learning (ML) techniques have been proposed as cost-effective and efficient ways to predict the influence of materials on properties, costs, and timelines of proposed mixtures [166]. To this aim, Shi et al. [163] used the artificial neural network (ANN) method to predict the mechanical and electrical properties of ECCs. Their study evidenced good agreement between the anticipated and observed outcomes, indicating that ANN models can forecast the properties of electrically conductive composites. The ANN technique was also used by [166] to predict the compressive strength of ECCs manufactured with fly ash and ground granulated blast furnace slag. While various ML algorithms were used to forecast various features of concrete, their use to predict self-healing ECC properties is not common and is challenging. Recently, in [167], the anisotropic–mechanical properties of 3DP-ECC were experimentally investigated and examined by means of ML prediction models like the non-dominated sorting genetic algorithm II (NSGA-II) to simultaneously optimize mechanical, environmental, and economic performances. A total of 114 sets of compressive strength data and 104 sets of flexural strength data were

used. As expected, 3DP-ECC showed a mechanical anisotropy particularly during flexural tests, attributed to weak interfaces and fiber orientation effects. The highest compressive strength was observed in the z direction. Moreover, 3DP-ECC displayed a lower compressive strength than cast ECCs whatever the loading direction. However, the flexural strength between the different samples was as follows: 3DP-z > 3DP-y > cast > 3DP-x. The grey relational analysis (GRA) results showed that the critical parameters influencing the mechanical properties of 3DP-ECC were the SCM-to-binder, aggregate-to-binder, and water-to-binder ratios, the fiber reinforcing index, and the loading direction, confirming the results of the papers analyzed in the previous chapters. Back-propagation artificial neural network (BPANN) models were interpreted with Shapley additive explanations (SHAP) and partial dependence plots (PDP) analyses. The results showed that the most significant parameters that impact the compressive strength of 3DP-ECC (R^2 = 0.999 and RMSE = 3.817 MPa when testing) were the water-to-binder ratio as well as the loading direction during flexural strength tests (R^2 = 0.998 and RMSE = 1.37 MPa when testing), as also shown in the previous chapters. In addition, the PDP analysis highlighted how each parameter influenced the anisotropic–mechanical properties of 3DP-ECC. However, further studies are still needed, as the specimen size and shape, curing age, and printing process parameters are also key factors that influence the mechanical properties of 3DP-ECC. Thus, their effects should also be taken into consideration in ML property prediction. Finally, this study mainly focused on the compressive strength and flexural strength of 3DP-ECC, omitting other important features like flowability and rheology, interlayer bond strength, and durability performance.

To sum up, machine learning techniques have confirmed that the crucial parameters influencing the mechanical properties of 3DP-ECC are as follows:

- SCM-to-binder ratio;
- Aggregate-to-binder and water-to-binder ratios;
- Fiber reinforcing index;
- Loading direction.

10. Conclusions and Perspectives

3DPC technology presents several benefits for the construction sector, such as a reductions in costs because of less labor (due to a lack of formwork, it is a direct process, and there are less risks for workers), as well as a decrease in energy consumption (lower movements of materials) and pollution (less waste produced). However, transferring these advantages to 3DP-ECC is not obvious. As previously discussed, the challenge of balancing conflicting requirements such as pumpability and buildability is not immediate due to the presence of fibers that should remain aligned in the filaments and ideally penetrate between the different layers to improve the interface strength.

The crucial parameters when 3D printing ECCs are as follows:

- Chemical stability of fibers in high-pH environments is mandatory;
- PE and PVA fibers that are 20–50 μm in Ø are commonly used for ECC manufacturing;
- Recycled aramid nanofibers seem promising as well;
- High aspect ratios are needed;
- Common dosages are 1–2 vol%;
- A high tensile strength and a rather low bond strength with the cementitious matrix are desirable;
- Fibers increase the yield stress at rest times, as well as the plastic viscosity and the dynamic yield stress;
- Fiber dispersion is of paramount importance, and rheological properties should be adapted;

- An optimized particle size distribution guarantees a good packing of particles and contributes to buildability;
- The open time should be 30-60 min and should be compatible with buildability;
- The order of mixing the products is fundamental in 3DP-ECC: first, solids are dry-mixed, then water and SP are added, and fibers are progressively introduced in the mix. Finally, the VMA is supplemented;
- The mix should have a low initial stiffness to be pumped and extruded, while the buildability requires a stiff material able to bear its own weight. Stiffness can be increased by CSA or sodium silicate additions;
- The extrusion speed should match the printing speed to control the shape and quality of printed filaments;
- Long delays between printing one filament above an existing are not advisable;
- When the nozzle standoff distance decreases by about 30%, the strain capacity of the same mixture can be increased by about 30%, while the tensile strength can be up to 39% higher;
- Internal curing should be considered to improve mechanical strength;
- Carbon curing can be actuated in ECCs, which can lower the pH of the matrix and make it more compatible with natural fibers.

Experimental tests and machine learning techniques showed that the crucial parameters influencing mechanical properties of 3DP-ECC are as follows:

- SCM-to-binder ratio;
- Aggregate-to-binder and water-to-binder ratios;
- Fiber reinforcing index;
- Loading direction.

Funding: This research received no external funding.

Conflicts of Interest: The author declares no conflicts of interest.

Abbreviations

The following abbreviations are used in this manuscript:

ECC	Engineered cementitious composite
SHCC	Strain-hardening cementitious composite
3D-SHCC	3D-printable strain-hardening cementitious composite
SCM	Supplementary cementitious material
PVA	Polyvinyl alcohol
PE	Polyethylene
PET	Polyethylene terephthalate
3DPC	3D printing process of concrete
3DP-ECC	3D-printed ECC
FA	Fly ash
SF	Silica fume
SP	Superplasticizer
HRWRA	High-range water-reducing agent
HPMC	Hydroxypropyl methyl cellulose
w/b	Water-to-binder
IBA	Incinerator bottom ash
OPC	Ordinary Portland cement
s/b	Sand-to-binder
UCCT	Uniaxial unconfined compression test
LC3	Limestone-calcined clay cement

CSA	Calcium sulphoaluminate
LL-ECC	Lightweight engineered cementitious composites
G	Graphite
MCMF	Milled carbon microfibers
CCMF	Chopped carbon microfibers
ML	Machine learning
ANN	Artificial neural network
NSGA-II	Sorting genetic algorithm II
GRA	Grey relational analysis
BPANN	Back-propagation artificial neural network
SHAP	Shapley additive explanations
PDP	Partial dependence plots
PEG	Polyethylene glycol

References

1. Mohajerani, A.; Hui, S.-Q.; Mirzababaei, M.; Arulrajah, A.; Horpibulsuk, S.; Abdul Kadir, A.; Rahman, M.T.; Maghool, F. Amazing Types, Properties, and Applications of Fibres in Construction Materials. *Materials* **2019**, *12*, 2513. [CrossRef]
2. Romualdi, J.P.; Batson, G.B. Mechanics of Crack Arrest in Concrete. *J. Eng. Mech. Div.* **1963**, *89*, 147–168. [CrossRef]
3. Romualdi, J.P.; Mandel, J.A. Tensile Strength of Concrete Affected by Uniformly Distributed and Closely Spaced Short Lengths of Wire Reinforcement. *ACI J. Proc.* **1964**, *61*, 657–672. [CrossRef]
4. Gencturk, B. Life-Cycle Cost Assessment of RC and ECC Frames Using Structural Optimization. *Earthq. Eng. Struct. Dyn.* **2013**, *42*, 61–79. [CrossRef]
5. Li, V.C. From Micromechanics to Structural Engineering-the Design of Cementitous Composites for Civil Engineering Applications. *Struct. Mech. Earthq. Eng.* **1993**, *10*, 37–48. [CrossRef]
6. Yu, K.; Li, L.; Yu, J.; Wang, Y.; Ye, J.; Xu, Q. Direct Tensile Properties of Engineered Cementitious Composites: A Review. *Constr. Build. Mater.* **2018**, *165*, 346–362. [CrossRef]
7. Li, V.C. Engineered Cementitious Composites (ECC). In *Bendable Concrete for Sustainable and Resilient Infrastructure*; Springer: Berlin/Heidelberg, Germany, 2019. [CrossRef]
8. Li, V.C. On engineered cementitious composites (ECC). *J. Adv. Concr. Technol.* **2003**, *1*, 215–230. [CrossRef]
9. Şahmaran, M.; Li, V.C. Durability Properties of Micro-Cracked ECC Containing High Volumes Fly Ash. *Cem. Concr. Res.* **2009**, *39*, 1033–1043. [CrossRef]
10. Li, V.C. Engineered Cementitious Composites (ECC) Material, Structural, and Durability Performance. In *Concrete Construction Engineering Handbook Series*; Nawy, E.G., Ed.; CRC Press: Boca Raton, FL, USA, 2008; ISBN 9780849374920.
11. Sarker, M.; Rahman, M.Z.; Abedin, M.J. Engineered cementitious composites: Design, structural and 3D printing applications. In *Comprehensive Materials Processing*, 2nd ed.; Elsevier: Amsterdam, The Netherlands, 2024; Volume 13, pp. 153–166. [CrossRef]
12. Lu, C.; Wang, J.; Leung, C.K.; Yao, Y.; Yu, B. Micromechanics-based model of single crack propagation in Engineered cementitious composites (ECC). *Constr. Build. Mater.* **2023**, *369*, 130519. [CrossRef]
13. Li, V.C.; Bos, F.P.; Yu, K.; McGee, W.; Ng, T.Y.; Figueiredo, S.C.; Nefs, K.; Mechtcherine, V.; Nerella, V.N.; Pan, J. On the emergence of 3D printable engineered, strain hardening cementitious composites (ECC/SHCC). *Cem. Concr. Res.* **2020**, *132*, 106038. [CrossRef]
14. Qudah, S.; Maalej, M. Application of engineered cementitious composites (ECC) in interior beam–column connections for enhanced seismic resistance. *Eng. Struct.* **2014**, *69*, 235–245. [CrossRef]
15. Zhang, R.; Matsumoto, K.; Hirata, T.; Ishizeki, Y.; Niwa, J. Application of PP-ECC in beam–column joint connections of rigid-framed railway bridges to reduce transverse reinforcements. *Eng. Struct.* **2015**, *86*, 146–156. [CrossRef]
16. Li, V.C.; Leung, C.K. Steady-State and Multiple Cracking of Short Random Fiber Composites. *J. Eng. Mech.* **1992**, *118*, 2246–2264. [CrossRef]
17. Dadkhah, M.; Tulliani, J.M. Damage Management of Concrete Structures with Engineered Cementitious Materials and Natural Fibers: A Review of Potential Uses. *Sustainability* **2022**, *14*, 3917. [CrossRef]
18. Oh, B.H.; Kabele, P. *Durability under Chemical Loads in: Durability of Strain-Hardening Fibre-Reinforced Cement-Based Composites (SHCC)*; Wittmann, F., Van Zijl, G., Eds.; Springer Science & Business Media: Berlin/Heidelberg, Germany, 2010; pp. 41–58. [CrossRef]
19. Toshiyuki, K.; Kabele, P.; Fukuyama, H.; Uchida, Y.; Suwada, H.; Slowik, V. Strain Hardening Cement Composites: Structural Design and Performance. In *State-of-the-Art Report of the RILEM Technical Committee 208-HFC, SC3*; Rokugo, K., Kanda, T., Eds.; Springer Science & Business Media: Berlin/Heidelberg, Germany, 2012. [CrossRef]

20. Wu, M.; Johannesson, B.; Geiker, M. A Review: Self-Healing in Cementitious Materials and Engineered Cementitious Composite as a Self-Healing Material. *Constr. Build. Mater.* **2012**, *28*, 571–583. [CrossRef]
21. van Overmeir, A.L.; Šavija, B.; Bos, F.P.; Schlangen, E. 3D printable strain hardening cementitious composites (3DP-SHCC), tailoring fresh and hardened state properties. *Constr. Build. Mater.* **2023**, *403*, 132924. [CrossRef]
22. Salet, T.; Ahmed, Z.; Bos, F.; Laagland, H. Design of a 3D printed concrete bridge by testing. *Virtual Phys. Prototyp.* **2018**, *13*, 222–236. [CrossRef]
23. Lim, S.; Buswell, R.; Le, T.; Austin, S.; Gibb, A.; Thorpe, T. Developments in construction-scale additive manufacturing processes. *Autom. Constr.* **2012**, *21*, 262–268. [CrossRef]
24. He, Z.; Chen, J.; Liu, Z.; Ma, Z. Analytical approach for bursting cracking analysis of post-tensioned anchorage zone. *Structures* **2023**, *52*, 401–409. [CrossRef]
25. Li, V.C.; Mishra, D.K.; Wu, H.-C. Matrix Design for Pseudo-Strain-Hardening Fibre Reinforced Cementitious Composites. *Mater. Struct.* **1995**, *28*, 586–595. [CrossRef]
26. Li, V.C.; Wang, S.; Wu, C. Tensile Strain-Hardening Behavior of Polyvinyl Alcohol Engineered Cementitious Composite (PVA-ECC). *Mater. J.* **2001**, *98*, 483–492. [CrossRef]
27. Li, V.C.; Wu, C.; Wang, S.; Ogawa, A.; Saito, T. Interface Tailoring for Strain-Hardening Polyvinyl Alcohol Engineered Cementitious Composite (PVA-ECC). *ACI Mater. J.* **2002**, *99*, 463–472. [CrossRef]
28. Myadaraboina, H.; Law, D.; Patnaikuni, I. Durability of Basalt Fibers in Concrete Medium. In *Australasia and Southeast Asia Conference in Structural Engineering and Construction (ASEA-SEC-2)*; ISEC Press: Fargo, ND, USA, 2014; pp. 445–450. [CrossRef]
29. Yin, S.; Tuladhar, R.; Shi, F.; Combe, M.; Collister, T.; Sivakugan, N. Use of Macro Plastic Fibres in Concrete: A Review. *Constr. Build. Mater.* **2015**, *93*, 180–188. [CrossRef]
30. Pelisser, F.; Montedo, O.R.K.; Gleize, P.J.P.; Roman, H.R. Mechanical Properties of Recycled PET Fibers in Concrete. *Mater. Res.* **2012**, *15*, 679–686. [CrossRef]
31. Lloyd, S. Steel Fibers in Concrete Floor Slabs. *Concr. Int.* **2014**, *36*, 47–49.
32. Caggiano, A.; Folino, P.; Lima, C.; Martinelli, E.; Pepe, M. On the mechanical response of Hybrid Fiber Reinforced Concrete with Recycled and Industrial Steel Fibers. *Constr. Build. Mater.* **2017**, *147*, 286–295. [CrossRef]
33. Men, P.; Wang, X.-M.; Liu, D.; Zhang, Z.; Zhang, Q.; Lu, Y. On use of polyvinylpyrrolidone to modify polyethylene fibers for improving tensile properties of high strength ECC. *Constr. Build. Mater.* **2024**, *4177*, 135354. [CrossRef]
34. Huo, Y.; Liu, T.; Lu, D.; Han, X.; Sun, H.; Chen, Z.; Li, Y.; Huang, J.; Yang, Y. Enhancing mechanical properties and crack resistance of high-strength SHCC/ECC for durable transportation through ethylene-vinyl acetate polymer modification. *Case Stud. Constr. Mater.* **2024**, *21*, e03878. [CrossRef]
35. Sun, H.; Wan, Y.; Xu, Z.; Huo, Y.; Jia, M.; Yang, Y. Exploring the potential of aramid nanofibers in advancing green-engineered cementitious composites. *Compos. B Eng.* **2025**, *305*, 112724. [CrossRef]
36. Yu, K.-Q.; Dai, J.-G.; Lu, Z.-D.; Leung, C.K. Mechanical Properties of Engineered Cementitious Composites Subjected to Elevated Temperatures. *J. Mater. Civ. Eng.* **2015**, *27*, 04014268. [CrossRef]
37. Yu, K.; Wang, Y.; Yu, J.; Xu, S. A Strain-Hardening Cementitious Composites with the Tensile Capacity up to 8%. *Constr. Build. Mater.* **2017**, *137*, 410–419. [CrossRef]
38. Yu, K.; Yu, J.; Lu, Z. Mechanical Characteristics of Ultra High Performance Strain Hardening Cementitious Composites. In *International Conference on Strain-Hardening Cement-Based Composites*; Springer: Dordrecht, The Netherlands, 2017; pp. 230–237.
39. Maalej, M.; Quek, S.T.; Zhang, J. Behavior of Hybrid-Fiber Engineered Cementitious Composites Subjected to Dynamic Tensile Loading and Projectile Impact. *J. Mater. Civ. Eng.* **2005**, *17*, 143–152. [CrossRef]
40. Maalej, M.; Quek, S.T.; Ahmed, S.F.U.; Zhang, J.; Lin, V.W.J.; Leong, K.S. Review of Potential Structural Applications of Hybrid Fiber Engineered Cementitious Composites. *Constr. Build. Mater.* **2012**, *36*, 216–227. [CrossRef]
41. Zhang, D.; Yu, J.; Wu, H.; Jaworska, B.; Ellis, B.R.; Li, V.C. Discontinuous Micro-Fibers as Intrinsic Reinforcement for Ductile Engineered Cementitious Composites (ECC). *Compos. Part. B Eng.* **2020**, *184*, 107741. [CrossRef]
42. Lei, D.; Jia, H.; Yu, L.; Li, Y.; Wu, Z.; Wang, B.; Zhou, A.; Qin, L.; Sun, J.; Wang, W.; et al. Recent developments in Low-Carbon Engineered Cementitious Composites (ECC). *J. Build. Eng.* **2025**, *100*, 111734. [CrossRef]
43. Shoji, D.; He, Z.; Zhang, D.; Li, V.C. The greening of engineered cementitious composites (ECC): A review. *Constr. Build. Mater.* **2022**, *327*, 126701. [CrossRef]
44. Hu, W.H.; Zhang, D.; Ftwi, E.; Ellis, B.R.; Li, V.C. Development of sustainable low carbon Engineered Cementitious Composites with waste polyethylene fiber, sisal fiber and carbonation curing. *Resour. Conserv. Recycl.* **2023**, *197*, 107096. [CrossRef]
45. Lin, Z.; Li, V.C. Crack Bridging in Fiber Reinforced Cementitious Composites with Slip-Hardening Interfaces. *J. Mech. Phys. Solids* **1997**, *45*, 763–787. [CrossRef]
46. Yang, E.-H.; Wang, S.; Yang, Y.; Li, V.C. Fiber-Bridging Constitutive Law of Engineered Cementitious Composites. *J. Adv. Concr. Technol.* **2008**, *6*, 181–193. [CrossRef]

47. Li, V.C. Large Volume, High-Performance Applications of Fibers in Civil Engineering. *J. Appl. Polym. Sci.* **2002**, *83*, 660–686. [CrossRef]
48. Katz, A.; Li, V.C. Inclination Angle Effect of Carbon Fibers in Cementitious Composites. *J. Eng. Mech.* **1995**, *121*, 1340–1348. [CrossRef]
49. Naaman, A.E.; Shah, S.P. Pull-out Mechanism in Steel Fiber-Reinforced Concrete. *J. Struct. Div.* **1976**, *102*, 1537–1548. [CrossRef]
50. Arnon, B. Role of Interfaces in Controlling Durability of Fiber-Reinforced Cements. *J. Mater. Civ. Eng.* **2000**, *12*, 2–7. [CrossRef]
51. Wang, S.; Li, V.C. Polyvinyl alcohol fiber reinforced engineered cementitious composites: Material design and performances. In Proceedings of the International RILEM Workshop on High Performance Fiber Reinforced Cementitious Composites in Structural Applications, Honolulu, HI, USA, 23–26 May 2005.
52. Yan, K.-T.; Wang, X.-P.; Ding, Y.; Li, L.-Z.; Bazarov, D.; Deng, B.-Y.; Nikolayevich, K.-S.; Yu, K.-Q. 3D-printed LC3-based lightweight engineered cementitious composites: Fresh state, harden material properties and beam performance. *J. Build. Eng.* **2024**, *93*, 109838. [CrossRef]
53. Xu, N.; Qian, Y. Effects of fiber volume fraction, fiber length, water-binder ratio, and nanoclay addition on the 3D printability of strain-hardening cementitious composites (SHCC). *Cem. Concr. Compos.* **2023**, *39*, 105066. [CrossRef]
54. Marcos-Meson, V.; Michel, A.; Solgaard, A.; Fischer, G.; Edvardsen, C.; Skovhus, T.L. Corrosion Resistance of Steel Fibre Reinforced Concrete—A Literature Review. *Cem. Concr. Res.* **2018**, *103*, 1–20. [CrossRef]
55. Khoshnevis, B.; Hwang, D.; Yao, K.-T.; Yeh, Z. Mega-scale fabrication by contour crafting. *Int. J. Ind. Syst. Eng.* **2006**, *1*, 301–320. [CrossRef]
56. Liu, D.; Zhang, Z.; Zhang, X.; Chen, Z. 3D printing concrete structures: State of the art, challenges, and opportunities. *Construct. Build. Mater.* **2023**, *405*, 133364. [CrossRef]
57. Marchment, T.; Sanjayan, J. Mesh reinforcing method for 3D concrete printing. *Autom. Construct.* **2020**, *109*, 102992. [CrossRef]
58. Classen, M.; Ungermann, J.; Sharma, R. Additive manufacturing of reinforced concrete—Development of a 3D printing technology for cementitious composites with metallic reinforcement. *Appl. Sci.* **2020**, *10*, 3791. [CrossRef]
59. Anton, A.; Reiter, L.; Wangler, T.; Frangez, V.; Flatt, R.J.; Dillenburger, B. A 3D concrete printing prefabrication platform for bespoke columns. *Autom. Construct.* **2021**, *122*, 103467. [CrossRef]
60. Wang, X.; Li, W.; Guo, Y.; Kashani, A.; Wang, K.; Ferrara, L.; Agudelo, I. Concrete 3D printing technology for sustainable construction: A review on raw material, concrete type and performance. *Dev. Built Environ.* **2024**, *17*, 100378. [CrossRef]
61. Sanjayan, J.G.; Nazari, A.; Nematollahi, B. *3D Concrete Printing Technology: Construction and Building Applications*, 1st ed.; Sanjayan, J.G., Nazari, A., Nematollahi, B., Eds.; Butterworth Heinemann: Oxford, UK, 2019. [CrossRef]
62. Perrot, A. *3D Printing of Concrete: State of the Art and Challenges of the Digital Construction Revolution*, 1st ed.; Perrot, A., Ed.; Wiley: Hoboken, NJ, USA, 2019. [CrossRef]
63. Brar, T.S.; Kamal, M.A.; Singh, S. *3D Concrete Printing Technology: Configuration with Green and Self-Healing Concrete*; Brar, T.S., Kamal, M.A., Singh, S., Eds.; Materials Research Forum LLC: Millersville, PA, USA, 2022. [CrossRef]
64. Grigoriadis, K.; Lee, G. *3D Printing and Material Extrusion in Architecture*; Grigoriadis, K., Lee, G., Eds.; DOM Publishers: Berlin, Germany, 2023; ISBN 9783869227504.
65. Tay, Y.W.D.; Lim, J.H.; Li, M.; Tan, M.J. Creating functionally graded concrete materials with varying 3D printing parameters. *Virtual Phys. Prototyp.* **2022**, *17*, 662–681. [CrossRef]
66. Chen, Y.; Chaves Figueiredo, S.; Li, Z.; Chang, Z.; Jansen, K.; Çopuroğlu, O.; Schlangen, E. Improving printability of limestone-calcined clay-based cementitious materials by using viscosity-modifying admixture. *Cement Concr. Res.* **2020**, *132*, 106040. [CrossRef]
67. Ashrafi, N.; Duarte, J.P.; Nazarian, S.; Meisel, N.A. Evaluating the relationship between deposition and layer quality in large-scale additive manufacturing of concrete. *Virtual Phys. Prototyp.* **2019**, *14*, 135–140. [CrossRef]
68. Soltan, D.G.; Li, V.C. A self-reinforced cementitious composite for building-scale 3d printing. *Cem. Concr. Compos.* **2018**, *90*, 1–13. [CrossRef]
69. Figueiredo, S.C.; Romero Rodriguez, C.; Ahmed, Z.Y.; Bos, D.; Xu, Y.; Salet, T.; Çopuroglu, O.; Schlangen, E.; Bos, F.P. An approach to develop printable strain hardening cementitious composites. *Mater. Des.* **2019**, *169*, 107651. [CrossRef]
70. Ogura, H.; Nerella, V.; Mechtcherine, V. Developing and testing of strain-hardening cement-based composites (shcc) in the context of 3d-printing. *Materials* **2018**, *11*, 1375. [CrossRef]
71. van Overmeir, A.; Figueiredo, S.; Šavija, B.; Bos, F.; Schlangen, E. Design and analysis of printable SHCC with optimized particle size distribution. *Constr. Build. Mater.* **2022**, *324*, 126411. [CrossRef]
72. Zhou, W.; Zhang, Y.; Ma, L.; Li, V.C. Influence of printing parameters on 3D printing engineered cementitious composites (3DP-ECC). *Cem. Concrete Compos.* **2022**, *130*, 104562. [CrossRef]
73. Zhu, B.; Pan, J.; Li, J.; Wang, P.; Zhang, M. Relationship between microstructure and strain-hardening behavior of 3D printed engineered cementitious composites. *Cem. Concr. Compos.* **2022**, *133*, 104677. [CrossRef]

74. Zafar, T.; Zafar, M.S.; Hojati, M. Exploring the 3D Printability of Engineered Cementitious Composites with Internal Curing for Resilient Construction in Arid Regions. *Materials* **2025**, *18*, 3327. [CrossRef] [PubMed]
75. Asghari, Y.; Mohammadyan-Yasouj, S.E.; Petrůc, M.; Ghandvar, H.; Koloor, S.S.R. 3D Printing and Implementation of Engineered Cementitious Composites—A Review. *Case Studies Constr. Mater.* **2024**, *21*, e03462. [CrossRef]
76. Zhou, W.; McGee, W.; Zhu, H.; Süleyman Gökçe, A.; Li, V.C. Time-dependent fresh properties characterization of 3D printing engineered cementitious composites (3DP-ECC): On the evaluation of buildability. *Cem. Concrete Compos.* **2022**, *133*, 104704. [CrossRef]
77. Fernández, F.; Jarabo, R.; Asensio, E.; Guerrero, A. Non-destructive tests to evaluate the self-healing capacity for a 3D printing ECC material. *Mater. Today Proc.* **2023**, *in press*. [CrossRef]
78. Zhu, B.; Pan, J.; Nematollahi, B.; Zhou, Z.; Zhang, Y.; Sanjayan, J. Development of 3D printable engineered cementitious composites with ultra-high tensile ductility for digital construction. *Mater. Des.* **2019**, *181*, 108088. [CrossRef]
79. Figueiredo, S.C.; Rodriguez, C.R.; Ahmed, Z.Y.; Bos, D.; Xu, Y.; Salet, T.; Çopuroglu, O.; Schlangen, E.; Bos, F. Mechanical Behavior of Printed Strain Hardening Cementitious Composites. *Materials* **2020**, *13*, 2253. [CrossRef]
80. Zhou, J.; Qian, S.; Sierra Beltran, M.G.; Ye, G.; van Breugel, K.; Li, V.C. Development of engineered cementitious composites with limestone powder and blast furnace slag. *Mater. Struct.* **2010**, *43*, 803–814. [CrossRef]
81. Khan, S.W.; Kamal, M.; Khan, F.A.; Gul, A.; Alam, M.; Shah, F.; Shahzada, K. Performance evaluation of the fresh and hardened properties of different PVA-ECC mixes: An experimental approach. *Case Stud. Constr. Mater.* **2023**, *18*, e01764. [CrossRef]
82. Pan, Z.; Wu, C.; Liu, J.; Wang, W.; Liu, J. Study on mechanical properties of cost- effective polyvinyl alcohol engineered cementitious composites (PVA-ECC). *Constr. Build. Mater.* **2015**, *78*, 397–404. [CrossRef]
83. Drescher, A.; Waters, A.; Rhoades, C. Arching in hoppers: I. Arching theories and bulk material flow properties. *Powder Technol.* **1995**, *84*, 165–174. [CrossRef]
84. Enstad, G. A Novel Theory on the Arching and Doming in Mass Flow Hoppers. Doctoral Dissertation, Norwegian Technical University, Trondheim, Norway, 1981.
85. Roussel, N. Rheological requirements for printable concretes. *Cem. Concr. Res.* **2018**, *112*, 76–85. [CrossRef]
86. Wangler, T.; Roussel, N.; Bos, F.P.; Salet, T.A.M.; Flatt, R.J. Digital concrete: A review. *Cem. Concr. Res.* **2019**, *123*, 105780. [CrossRef]
87. Roussel, N. A thixotropy model for fresh fluid concretes: Theory, validation and applications. *Cem. Concr. Res.* **2006**, *36*, 1797–1806. [CrossRef]
88. Perrot, A.; Rangeard, D.; Pierre, A. Structural built-up of cement-based materials used for 3D-printing extrusion techniques. *Mater. Struct.* **2016**, *49*, 1213–1220. [CrossRef]
89. Buswell, R.A.; Leal De Silva, W.R.; Jones, S.Z.; Dirrenberger, J. 3D printing using concrete extrusion: A roadmap for research. *Cem. Concr. Res.* **2018**, *112*, 37–49. [CrossRef]
90. Wolfs, R.J.M.; Bos, F.P.; Salet, T.A.M. Early age mechanical behaviour of 3D printed concrete: Numerical modelling and experimental testing. *Cem. Concr. Res.* **2018**, *106*, 103–116. [CrossRef]
91. Rahul, A.V.; Mohan, M.K.; De Schutter, G.; Van Tittelboom, K. 3D printable concrete with natural and recycled coarse aggregates: Rheological, mechanical and shrinkage behaviour. *Cem. Concr. Compos.* **2022**, *125*, 104311. [CrossRef]
92. Nerella, V.N.; Krause, M.; Mechtcherine, V. Direct printing test for buildability of 3D-printable concrete considering economic viability. *Automat. Constr.* **2020**, *109*, 102986. [CrossRef]
93. Suiker, A.S.J. Mechanical performance of wall structures in 3D printing processes: Theory, design tools and experiments. *Int. J. Mech. Sci.* **2018**, *137*, 145–170. [CrossRef]
94. Zhang, Y.; Zhang, Y.; Liu, G.; Yang, Y.; Wu, M.; Pang, B. Fresh properties of a novel 3D printing concrete ink. *Constr. Build. Mater.* **2018**, *174*, 263–271. [CrossRef]
95. Le, T.T.; Austin, S.A.; Lim, S.; Buswell, R.A.; Gibb, A.G.F.; Thorpe, T. Mix design and fresh properties for high-performance printing concrete. *Mater. Struct.* **2012**, *45*, 1221–1232. [CrossRef]
96. Kazemian, A.; Yuan, X.; Cochran, E.; Khoshnevis, B. Cementitious materials for construction-scale 3D printing: Laboratory testing of fresh printing mixture. *Constr. Build. Mater.* **2017**, *145*, 639–647. [CrossRef]
97. Panda, B.; Tan, M.J. Rheological behavior of high volume fly ash mixtures containing micro silica for digital construction application. *Mater. Lett.* **2019**, *237*, 348–351. [CrossRef]
98. Weng, Y.; Li, M.; Tan, M.J.; Qian, S. Design 3D printing cementitious materials via Fuller Thompson theory and Marson-Percy model. *Constr. Build. Mater.* **2018**, *163*, 600–610. [CrossRef]
99. Joh, C.; Lee, J.; Bui, T.Q.; Park, J.; Yang, I. Buildability and mechanical properties of 3D printed concrete. *Materials* **2020**, *13*, 4919. [CrossRef]
100. Ahmed, S.; Yehia, S. Evaluation of workability and structuration rate of locally developed 3D printing concrete using conventional methods. *Materials* **2022**, *15*, 1243. [CrossRef]
101. Yuan, Q.; Li, Z.; Zhou, D.; Huang, T.; Huang, H.; Jiao, D.; Shi, C. A feasible method for measuring the buildability of fresh 3D printing mortar. *Constr. Build. Mater.* **2019**, *227*, 116600. [CrossRef]

102. Liu, Q.; Jiang, Q.; Huang, M.; Xin, J.; Chen, P.; Wu, S. Modifying effect of anionic polyacrylamide dose for cement-based 3DP materials: Printability and mechanical performance tests. *Constr. Build. Mater.* **2022**, *330*, 127156. [CrossRef]
103. Casagrande, L.; Esposito, L.; Menna, C.; Asprone, D.; Auricchio, F. Effect of testing procedures on buildability properties of 3D-printable concrete. *Constr. Build. Mater.* **2020**, *245*, 118286. [CrossRef]
104. Wolfs, R.J.M.; Bos, F.P.; Salet, T.A.M. Triaxial compression testing on early age concrete for numerical analysis of 3D concrete printing. *Cem. Concr. Compos.* **2019**, *104*, 103344. [CrossRef]
105. Panda, B.; Lim, J.H.; Tan, M.J. Mechanical properties and deformation behaviour of early age concrete in the context of digital construction. *Compos. B Eng.* **2019**, *165*, 563–571. [CrossRef]
106. Wang, Y.; Jiang, Y.; Pan, T.; Yin, K. The synergistic effect of ester-ether copolymerization thixo-tropic superplasticizer and nano-clay on the buildability of 3D printable cementitious materials. *Materials* **2021**, *14*, 4622. [CrossRef]
107. Tripathi, A.; Nair, S.A.O.; Neithalath, N. A comprehensive analysis of buildability of 3D-printed concrete and the use of bi-linear stress-strain criterion-based failure curves towards their prediction. *Cem. Concr. Compos.* **2022**, *128*, 104424. [CrossRef]
108. Zhu, B.; Nematollahi, B.; Pan, J.; Zhang, Y.; Zhou, Z.; Zhang, Y. 3D concrete printing of permanent formwork for concrete column construction. *Cem. Concr. Compos.* **2021**, *121*, 104039. [CrossRef]
109. Jayathilakage, R.; Rajeev, P.; Sanjayan, J.G. Yield stress criteria to assess the buildability of 3D concrete printing. *Constr. Build. Mater.* **2020**, *240*, 117989. [CrossRef]
110. Kruger, J.; Zeranka, S.; van Zijl, G. 3D concrete printing: A lower bound analytical model for buildability performance quantification. *Automat. Constr.* **2019**, *106*, 102904. [CrossRef]
111. Ivanova, I.; Ivaniuk, E.; Bisetti, S.; Nerella, V.N.; Mechtcherine, V. Comparison between methods for indirect assessment of buildability in fresh 3D printed mortar and concrete. *Cem. Concr. Res.* **2022**, *156*, 106764. [CrossRef]
112. Tramontin Souza, M.; Maia Ferreira, I.; Guzi De Moraes, E.; Senff, L.; Arcaro, S.; Castro Pessôa, J.R.; Ribeiro, M.J.; Novaes De Oliveira, A.P. Role of chemical admixtures on 3D printed Portland cement: Assessing rheology and buildability. *Constr. Build. Mater.* **2022**, *314*, 125666. [CrossRef]
113. Ma, G.; Li, Z.; Wang, L. Printable properties of cementitious material containing copper tailings for extrusion based 3D printing. *Constr. Build. Mater.* **2018**, *162*, 613–627. [CrossRef]
114. Ye, J.; Cui, C.; Yu, J.; Yu, K.; Dng, F. Effect of polyethylene fiber content on workability and mechanical-anisotropic properties of 3D printed ultra-high ductile concrete. *Constr. Build. Mater.* **2021**, *281*, 122586. [CrossRef]
115. Kruger, J.; Zeranka, S.; Van Zijl, G. An ab initio approach for thixotropy characterisation of (nanoparticle-infused) 3D printable concrete. *Constr. Build. Mater.* **2019**, *224*, 372–386. [CrossRef]
116. Ge, Y.; Yao, J. Influence of FA and HPMC on the fresh properties and anisotropy of 3D printing engineered cementitious composites (3DP-ECC). *Mater. Lett.* **2025**, *381*, 137748. [CrossRef]
117. Lomboy, G.R.; Wang, X.; Wang, K. Rheological behavior and formwork pressure of SCC, SFSCC, and NC mixtures. *Cem. Concr. Compos.* **2014**, *54*, 110–116. [CrossRef]
118. Liu, H.; Xiao, J.; Ding, T. Flexural performance of 3D-printed composite beams with ECC and recycled fine aggregate concrete: Experimental and numerical analysis. *Eng. Struct.* **2023**, *283*, 115865. [CrossRef]
119. Yu, K.; McGee, W.; Ng, T.Y.; Zhu, H.; Li, V.C. 3D-printable engineered cementitious composites (3DP-ECC): Fresh and hardened properties. *Cem. Concr. Res.* **2021**, *143*, 106388. [CrossRef]
120. Hu, C.; de Larrard, F.; Sedran, T.; Boulay, C.; Bosc, F.; Deflorenne, F. Validation of BTRHEOM, the new rheometer for soft-to-fluid concrete. *Mater. Struct.* **1996**, *29*, 620–631. [CrossRef]
121. Pi, Y.; Lu, C.; Yao, Y.; Li, B. A rheological-based printability assessment method for 3D printing Engineered Cementitious Composites considering fiber dispersion. *Case Stud. Constr. Mater.* **2024**, *20*, e02898. [CrossRef]
122. Jaggi, S.; Sharma, P.K. Fresh, Compressive and Direct-Tensile characterization of Engineered Cementitious Composite. *IOP Conf. Ser. Earth Environ. Sci.* **2024**, *1327*, 012004. [CrossRef]
123. Kan, L.; Shi, R.; Zhu, J. Effect of fineness and calcium content of fly ash on the mechanical properties of engineered cementitious composites (ECC). *Constr. Build. Mater.* **2019**, *209*, 476–484. [CrossRef]
124. Yu, J.; Leung, C.K. Impact of 3D printing direction on mechanical performance of strain-hardening cementitious composite (SHCC). In Proceedings of the First RILEM International Conference on Concrete and Digital Fabrication—Digital Concrete, Zurich, Switzerland, 10–12 September 2018; Springer: Cham, Switzerland, 2018; pp. 255–265. [CrossRef]
125. Pourchez, J.; Ruot, B.; Debayle, J.; Pourchez, E.; Grosseau, P. Some aspects of cellulose ethers influence on water transport and porous structure of cement-based materials. *Cem. Concr. Res.* **2010**, *40*, 242–252. [CrossRef]
126. Jenni, A.; Holzer, L.; Zurbriggen, R.; Herwegh, M. Influence of polymers on microstructure and adhesive strength of cementitious tile adhesive mortars. *Cem. Concr. Res.* **2005**, *35*, 35–50. [CrossRef]
127. Jenni, A.; Zurbriggen, R.; Holzer, L.; Herwegh, M. Changes in microstructures and physical properties of polymer-modified mortars during wet storage. *Cem. Concr. Res.* **2006**, *36*, 79–90. [CrossRef]

128. Kan, L.; Kong, N.; Wang, F. Effects of thickener on macro- and meso-mechanical properties of ECC. *Case Stud. Constr. Mater.* **2023**, *19*, e02292. [CrossRef]
129. Yu, J.; Xu, F.; Zhang, H.; Ye, J.; Yu, J.; Dai, J.-G. Yiwei Weng Leveraging incinerator bottom ash for mitigating early age shrinkage in 3D printed engineered cementitious composites. *Cem. Concr. Compos.* **2025**, *157*, 105933. [CrossRef]
130. Sun, J.; Aslani, F.; Lu, J.; Wang, L.; Huang, Y.; Ma, G. Fibre-reinforced lightweight engineered cementitious composites for 3D concrete printing. *Ceram. Int.* **2021**, *47*, 27107–27121. [CrossRef]
131. Du, Q.; Qian, Y. Effects of printing patterns and loading directions on fracture behavior of 3D printed Strain-Hardening Cementitious Composites. *Eng. Fract. Mech.* **2024**, *304*, 110155. [CrossRef]
132. Bai, M.; Xiao, J.; Ding, T.; Yu, K. Interfacial bond properties between 3D printed engineered cementitious composite (ECC) and post-cast concrete. *Cem. Concr. Compos.* **2025**, *157*, 105897. [CrossRef]
133. Xiao, J.; Bai, M.; Wu, Y.; Duan, Z.; Qin, J. Interlayer bonding strength and pore characteristics of 3D printed engineered cementitious composites (ECC). *J. Build. Eng.* **2024**, *84*, 108559. [CrossRef]
134. Scrivener, K.; Martirena, F.; Bishnoi, S.; Maity, S. Calcined clay limestone cements (LC3). *Cem. Concr. Res.* **2018**, *114*, 49–56. [CrossRef]
135. Antoni, M.; Rossen, J.; Martirena, F.; Scrivener, K. Cement substitution by a combination of metakaolin and limestone. *Cem. Concr. Res.* **2012**, *42*, 1579–1589. [CrossRef]
136. Abdelzaher, M.A.; Hamouda, A.S.; Ismail, I.M.; El-Sheikh, M.A. Nano titania reinforced limestone cement: Physico-mechanical investgation. *Key Eng. Mater.* **2018**, *786*, 248–257. [CrossRef]
137. Zhang, D.; Jaworska, B.; Zhu, H.; Dahlquist, K.; Li, V.C. Engineered Cementitious Composites (ECC) with limestone calcined clay cement (LC3). *Cem. Concr. Compos.* **2020**, *114*, 103766. [CrossRef]
138. Wang, Y.; Chen, M.; Zhang, T.; Zhang, M. Hardening properties and microstructure of 3D printed engineered cementitious composites based on limestone calcined clay cement. *Cem. Concr. Compos.* **2024**, *152*, 105641. [CrossRef]
139. Zhou, W.; Zhu, H.; Hu, W.-H.; Wollaston, R.; Li, V.C. Low-carbon, expansive engineered cementitious composites (ECC) in the context of 3D printing. *Cem. Concr. Compos.* **2024**, *148*, 105473. [CrossRef]
140. Liu, H.; Laflamme, S.; D'Alessandro, A.; Ubertini, F. 3D printed self-sensing cementitious composites using graphite and carbon microfibers. *Meas. Sci. Technol.* **2024**, *35*, 085105. [CrossRef]
141. Aslani, F.; Dale, R.; Hamidi, F.; Valizadeh, A. Mechanical and shrinkage performance of 3D-printed rubberised engineered cementitious composites. *Constr. Build. Mater.* **2022**, *339*, 127665. [CrossRef]
142. Ma, G.; Li, Z.; Wang, L.; Wang, F.; Sanjayan, J. Mechanical anisotropy of aligned fiber reinforced composite for extrusion-based 3D printing. *Constr. Build. Mater.* **2019**, *202*, 770–783. [CrossRef]
143. Du, G.; Sun, Y.; Qian, Y. Nature-inspired approach for enhancing the fracture performance of 3D printed strain-hardening cementitious composites (3DP-SHCC). *Eng. Struct.* **2025**, *322*, 119074. [CrossRef]
144. Zhou, W.; McGee, W.; Gökçe, H.S.; Li, V.C. A bio-inspired solution to alleviate anisotropy of 3D printed engineered cementitious composites (3DP-ECC): Knitting/tilting filaments. *Autom. Constr.* **2023**, *155*, 105051. [CrossRef]
145. Zhu, B.; Pan, J.; Zhou, Z.; Cai, J. Mechanical properties of engineered cementitious composites beams fabricated by extrusion-based 3D printing. *Eng. Struc.* **2021**, *238*, 112201. [CrossRef]
146. Bai, M.; Wu, Y.; Xiao, J.; Ding, T.; Yu, K. Workability and hardened properties of 3D printed engineered cementitious composites incorporating recycled sand and PE fibers. *J. Build. Eng.* **2023**, *71*, 106477. [CrossRef]
147. Zhu, L.L.; Yao, J.; Zhao, Y.; Ruan, W.; Yang, G.; Guan, X.M. Effects of composite cementation system on rheological and working performances of fresh 3D-printable engineered cementitious composites. *J. Build. Eng.* **2023**, *65*, 105801. [CrossRef]
148. Zhang, Y.; Aslani, F. Development of fibre reinforced engineered cementitious composite using polyvinyl alcohol fibre and activated carbon powder for 3D concrete printing. *Constr. Build. Mater.* **2021**, *201*, 124453. [CrossRef]
149. Le, T.T.; Austin, S.A.; Lim, S.; Buswell, R.A.; Law, R.; Gibb, A.G.F.; Thorpe, T. Hardened properties of high-performance printing concrete. *Cem. Concr. Res.* **2012**, *42*, 558–566. [CrossRef]
150. Nerella, V.N.; Hempel, S.; Mechtcherine, V. Effects of layer-interface properties on mechanical performance of concrete elements produced by extrusion-based 3Dprinting. *Constr. Build. Mater.* **2019**, *205*, 586–601. [CrossRef]
151. Al-Gemeel, A.N.; Zhuge, Y.; Youssf, O. Experimental investigation of basalt textile reinforced engineered cementitious composite under apparent hoop tensile loading. *J. Build. Eng.* **2019**, *23*, 270–279. [CrossRef]
152. Al-Gemeel, A.N.; Zhuge, Y.; Youssf, O. Use of hollow glass microspheres and hybrid fibres to improve the mechanical properties of engineered cementitious composite. *Constr. Build. Mater.* **2018**, *171*, 858–870. [CrossRef]
153. Lu, C.; Pan, J.; Luo, B.; Li, Z.; Leung, C.K.Y. Correlation of flaw structure and cracking behavior in SHCC with X-ray CT scanning technique. *Constr. Build. Mater.* **2022**, *331*, 127296. [CrossRef]
154. Hao, Z.; Lu, C.; Li, Z. Highly accurate and automatic semantic segmentation of multiple cracks in engineered cementitious composites (ECC) under dual premodification deep-learning strategy. *Cem. Concr. Res.* **2023**, *165*, 107066. [CrossRef]

155. Dong, B.; Lu, C.; Pan, J.; Shan, Q.; Yin, W. Mechanical behavior of a novel precast beam-to-column connection with U-shaped bars and engineered cementitious composites. *Adv. Struct. Eng.* **2018**, *21*, 1963–1976. [CrossRef]
156. Pang, Z.; Lu, C.; Li, B.; Wang, J. A multiscale model for quantifying fiber orientation effects on the tensile properties of 3D printed Engineered Cementitious Composites (3DP-ECC). *J. Build. Eng.* **2023**, *68*, 106090. [CrossRef]
157. He, B.; Zhang, H.; Zhu, X.; Zheng, Q.; Onuaguluchi, O.; Banthia, N.; Jiang, Z. Thermal-dependent brittleness effect of ultra-high performance concrete exposed to cryogenic flexural loads by acoustic emission evaluation. *Cem. Concr. Compos.* **2023**, *139*, 105056. [CrossRef]
158. Hou, M.; Zhang, D.; Li, V.C. Crack width control and mechanical properties of low carbon engineered cementitious composites (ECC). *Constr. Build. Mater.* **2022**, *348*, 128692. [CrossRef]
159. Li, M.; Li, V.C. Rheology, fiber dispersion, and robust properties of Engineered Cementitious Composites. *Mater. Struct.* **2013**, *46*, 405–420. [CrossRef]
160. El-Dieb, A.S.; El-Maaddawy, T.A.; Mahmoud, A.A.M. Water-soluble polymers as self-curing agent in cement mixes. *Adv. Cem. Res.* **2012**, *24*, 291–299. [CrossRef]
161. Dixit, A.; Gupta, S.; Dai Pang, S.; Kua, H.W. Waste valorisation using biochar for cement replacement and internal curing in ultra-high performance concrete. *J. Clean. Prod.* **2019**, *238*, 117876. [CrossRef]
162. Wang, T.; Tang, Y.; Qin, S.; Li, G.; Wu, H.; Leung, C.K.Y. Sustainable and mechanical properties of Engineered Cementitious Composites with biochar: Integrating micro- and macro-mechanical insight. *Cem. Concr. Compos.* **2025**, *155*, 105813. [CrossRef]
163. Shi, L.; Lin, S.; Lu, Y.; Ye, L.; Zhang, Y. Artificial neural network based mechanical and electrical property prediction of engineered cementitious composites. *Constr. Build. Mater.* **2018**, *174*, 667–674. [CrossRef]
164. Le, V.-G.; Nguyen, M.-K.; Nguyen, H.-L.; Lin, C.; Hadi, M.; Quang Hung, N.T.; Hoang, H.-G.; Nguyen, K.N.; Tran, H.-T.; Hou, D.; et al. A comprehensive review of micro- and nano-plastics in the atmosphere: Occurrence, fate, toxicity, and strategies for risk reduction. *Sci. Total Environ.* **2023**, *904*, 166649. [CrossRef]
165. Tükoğlu, G.C.; Khomarloo, N.; Mohsenzadeh, E.; Gospodinova, D.N.; Neznakomova, M.; Salaün, F. PVA-Based Electrospun Materials—A Promising Route to Designing Nanofiber Mats with Desired Morphological Shape—A Review. *Int. J. Mol. Sci.* **2024**, *25*, 1668. [CrossRef]
166. Shanmugasundaram, N.; Praveenkumar, S.; Gayathiri, K.; Divya, S. Prediction on compressive strength of engineered cementitious composites using machine learning approach. *Constr. Build. Mater.* **2022**, *342*, 127933. [CrossRef]
167. Chen, W.; Liang, L.; Ye, J.; Liu, L.; Ukrainczyk, N.; Yin, L.; Yu, J.; Yu, K. Machine learning-enabled performance-based design of three-dimensional printed engineered cementitious composites. *Eng. Appl. Artif. Intell.* **2025**, *161*, 112117. [CrossRef]